Early evolutionary stage of protoplanetary disk and dust growth

川崎, 良寛

出版情報：Kyushu University, 2023, 博士（理学）, 課程博士
バージョン：
権利関係：

Early evolutionary stage of protoplanetary disk and dust growth

Yoshihiro Kawasaki

Department of Earth and Planetary Sciences, Graduate School of Science, Kyushu University

26 February 2024

ABSTRACT

Protoplanetary disks are formed around the protostars. These disks are composed of gas and solid small particles called dust particles. In disks, the collisional growth of small dust particles is considered the initiation of planet formation. In the past decade, observations with the Atacama Large Millimeter/Submillimeter Array (ALMA) have reported disks exhibiting various structures, such as spiral and ring structures. These structures in disks imply the growth of dust particles and the presence of planets. Disks with such structures are considered to be relatively evolved disks (Class II/III). On the other hand, observations of younger disks (Class 0/I) have also been conducted in recent years. Observational results suggesting dust growth in early evolutionary stage disks have been reported; however, the aforementioned structures are rarely observed in Class 0/I disks. To unravel the planet formation process, it is crucial to understand how dust particles, which are the material for planets, grow and distribute spatially within disks.

The collisional growth process of dust particles depends on the composition, internal structure, and collisional velocity of dust particles. Furthermore, dust particles experience motion influenced by aerodynamic drag with the gas within a disk. Therefore, to understand the collisional growth and motion of dust particles, it is important to consider the gas density and temperature distribution within the disk. The formation and evolution processes of disks have been studied using numerical simulations. Three-dimensional numerical simulations starting with the gravitational collapse of the molecular cloud core, which is the progenitor of both the protostar and the disk, have demonstrated the formation of a disk together with a protostar. Furthermore, the mass ejection reported in observations, known as outflows (disk winds), has also been reproduced in simulations. Recently, three-dimensional numerical simulations considering dust have been performed. These simulations show the difference in the spatial distribution between gas and dust and the impact of the disk evolution. However, three-dimensional numerical simulations have high computational costs, making long-term calculations challenging. Thus, one-dimensional calculations have been used to investigate long-term disk evolution. Although a disk wind plays an important role in mass loss from a disk and angular momentum transport, there is little research on one-dimensional calculations that consider a disk wind from the early evolutionary stages of disk formation. Furthermore, the impact of changes in disk structure due to disk winds on the growth and spatial distribution of dust particles remains poorly understood. Therefore, in this study, we conduct one-dimensional calculations, including the disk formation process, to investigate the impact of a disk wind on disk evolution and the evolution of dust sizes by comparing calculations with and without a disk wind.

In disk evolution calculations, episodic accretions (or outbursts) occur repeatedly as reported in previous studies, regardless of the presence of a disk wind. Fluctuations of the surface density and disk temperature are seen for the inner disk region due to outbursts. The time interval between outbursts in the case with disk wind is shorter than that in the case without disk wind. Furthermore, the calculation with disk wind resulted in a larger disk size. Regarding the growth of dust particles,

during the infall phase, there is not a significant difference in the presence or absence of a disk wind, and dust particles grow to approximately 1-10 cm. Inside the H_2O snowline, the maximum dust size is limited by the collisional fragmentation of dust particles. On the other hand, outside the snowline, the maximum dust size is almost determined by the radial drift of dust particles. After the infall phase, the disk temperature decreases due to a disk wind, and the snowline migrates inward. As a result, the dust particles can grow larger than 10 cm. Therefore, it is found that a disk wind is crucial for dust growth or planet formation after the infall phase.

CONTENTS

1 Introduction

1.1 Star and disk formation processes

The elucidation of planet formation processes has been a longstanding question in the fields of astronomy and planetary science. In interstellar space, there are microscopic solid particles called dust (particles). It is thought that the collisional growth of these dust particles is the initiation of planet formation. The process of planet formation is believed to take place in protoplanetary disks composed of gas and dust particles (Testi et al. 2014). The protoplanetary disks are formed as part of the star formation process.

In interstellar space, there are regions with relatively high density called molecular clouds. Within these clouds, there are regions with even higher density, gravitationally bound, known as molecular cloud cores (Tokuda et al. 2020). The collapse of the molecular cloud cores due to self-gravity leads to the formation of protostars at their centers (Inutsuka 2012). Molecular cloud cores possess angular momentum, and as they contract, the rotation speed of the gas increases due to the conservation of angular momentum. When the central mass becomes massive, a balance between gravity and centrifugal force prevents the gas from infalling directly to the center. As a result, the disks form around the central stars. After the formation of a disk, the envelope gas accretes through the disk to the central star. It is considered that the gas in the disks loses angular momentum due to magnetic hydrodynamic effects and gravitational torque, leading to accretion onto the stars (Machida & Matsumoto 2011; Tomida et al. 2017). Since planet formation occurs within the disks, understanding the formation and evolution of the disks is important.

1.2 Dust particles in protoplanetary disks

As mentioned above, the planet formation is considered to begin from the collisional growth of the dust particles in protoplanetary disks. When dust particles collide with each other, whether the colliding particles stick to each other depends on the composition, the internal structure, and the collision velocity of dust particles. The collisional processes of dust particles have been investigated through laboratory experiments and numerical simulations. The fragmentation velocity of the dust particles has been estimated from these experiments (Blum & Münch 1993; Wurm et al. 2005; Langkowski et al. 2008) and simulations (Dominik & Tielens 1997; Wada et al. 2013; Hasegawa et al. 2021, 2023; Arakawa et al. 2023a,b). Water-ice dust particles tend to stick together more easily than silicate dust particles. The collisional fragmentation velocity for silicate dust particles is estimated to be around $1-10$ m/s, while for water-ice dust particles, it is estimated to be around $10-80$ m/s (Wada et al. 2009, 2013). Thus, the composition of dust particles is one of the crucial elements for understanding the process of planet formation.

To explain planet formation, we need to understand the motion of dust particles within the disk. Dust particles are influenced by aerodynamic friction force from the disk gas (Weidenschilling 1977), described by,

$$\mathbf{F}_{\mathrm{drag}} = -\frac{\mathbf{v}_{\mathrm{d}} - \mathbf{v}_{\mathrm{g}}}{t_{\mathrm{s}}}, \tag{1}$$

where $\mathbf{v}_{\mathrm{d}}$ is the dust velocity, $\mathbf{v}_{\mathrm{g}}$ is the gas velocity, and t_{s} is the stopping time of dust particles. As this equation indicates, the friction force acts in the opposite direction to the relative velocity between dust and gas. The stopping time t_{s} represents the typical time for the aerodynamic friction force to act and depends on the internal density and size of the dust particles. The Stokes number $\mathrm{St} = \Omega t_{\mathrm{s}}$, which is the stopping time normalized by the orbital period Ω of the disk, is used for studies of dust evolution in a disk. A Dust particle with a Stokes number less than unity is well-coupled with the disk gas, while a dust particle with a Stokes number greater than unity is decoupled with the disk gas. An example of the motion of dust particles subjected to aerodynamic friction force is radial drift. Large dust particles with the Stokes number around unity are strongly affected by the headwind from the gas and lose their angular momentum. As a result, these dust particles drift toward the center and infall to the central star before they grow into planets. This problem is called "the dust radial drift barrier". Therefore, the density, temperature, and chemical structure of the disk gas are crucial for understanding the growth and motion of dust particles.

1.3 Observation of protoplanetary disks

In recent decades, improvements in observational techniques and accuracy have unveiled the structures of protoplanetary disks. Figure 1 shows the results from the Atacama Large Millimeter/Submillimeter Array (ALMA) observations focused on Class II and subsequent evolved disks (Andrews et al. 2018). Various structures within the disks, such as spirals and rings, have been detected. These structures suggest the growth and accumulation of dust particles within the disks and the possible presence of planets. The formation processes of such structures within disks continue to be subjects of ongoing debate. For instance, theories propose that structures could be created when growth dust particles are trapped in regions with maximum pressure (Whipple 1972; Adachi et al. 1976) or that planets are formed due to gravitational instability (Coradini et al. 1981; Johansen et al. 2007).

Observations targeting young Class 0/I disks have been conducted in recent years. Figure 2 represents the observational results of the edisk project (Ohashi et al. 2023a). In comparison to Class II disks (Fig. 1), disks with observable structures are rarely detected. The reasons for these smooth disks are considered to be that disks at this stage are optically thick, making structures less distinct, and planets have not yet formed. Additionally, it is suggested from these observations that the structures of Class II disks might have formed in a short time after Class 0/I disks. On the other hand, Sheehan et al. (2020) detected the sub-structures in Class 0/I disks while their origin is less clear. Observational results also indicate that dust particles are growing in Class 0/I disks (Ohashi et al. 2023b; Shoshi et al. 2023; Liu et al. 2023). Therefore, understanding the dust growth in Class 0/I disks and determining when planet formation begins after disk formation are crucial questions.

1.4 Theoretical studies of disk formation and evolution

Many studies on the early star formation stage have been conducted using multi-dimensional numerical simulations. Non-ideal magnetohydrodynamic simulations with molecular cloud cores as initial conditions demonstrated the formation processes of protostars and disks (Machida et al. 2010; Machida & Matsumoto 2011; Tsukamoto et al. 2020; Xu & Kunz 2021a,b). The disks become gravitationally unstable, leading to the development of spiral arms and angular momentum transport due to gravitational torque (Tomida et al. 2017). Additionally, outflows, which transport the mass and angular momentum from the central region of the cores, are also reproduced in these simulations (Tomida et al. 2013; Machida & Basu 2019).

Recently, multi-dimensional numerical simulations, including dust particles, have been performed (Lebreuilly et al. 2019, 2020; Tsukamoto et al. 2021a,b; Koga et al. 2022; Koga & Machida 2023; Marchand et al. 2023). These simulations have shown differences in spatial distribution between gas and dust (Lebreuilly et al.

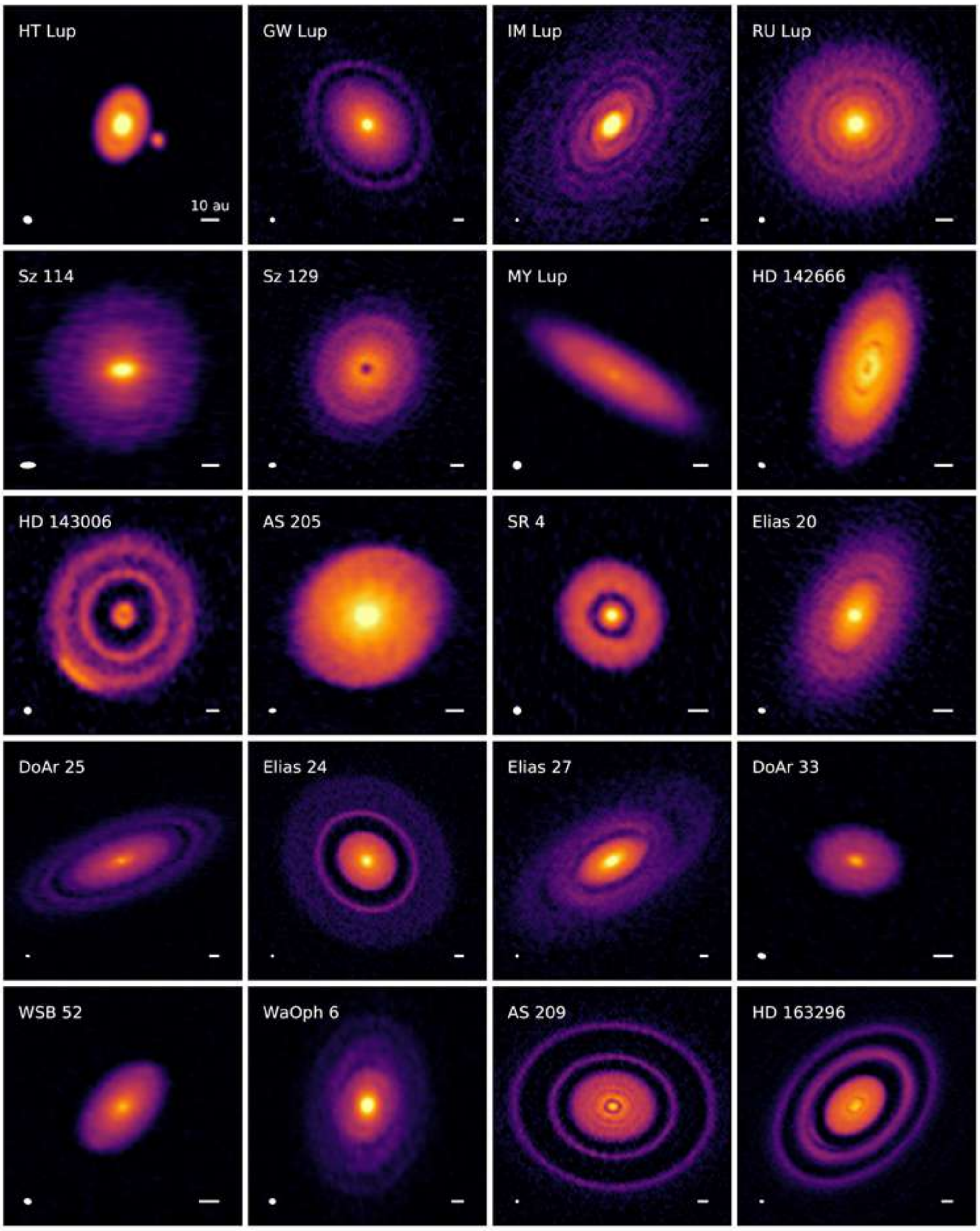

Figure 1. The observation results of protoplanetary disks performed by the DSHARP project.

2020), and impacts of the growth of dust particles on the disk evolution and outflow activity (Tsukamoto et al. 2023). Multidimensional numerical simulations are a highly useful tool in the study of the formation and evolution of stars and disks. However, the calculation cost of these simulations is expensive and it is difficult

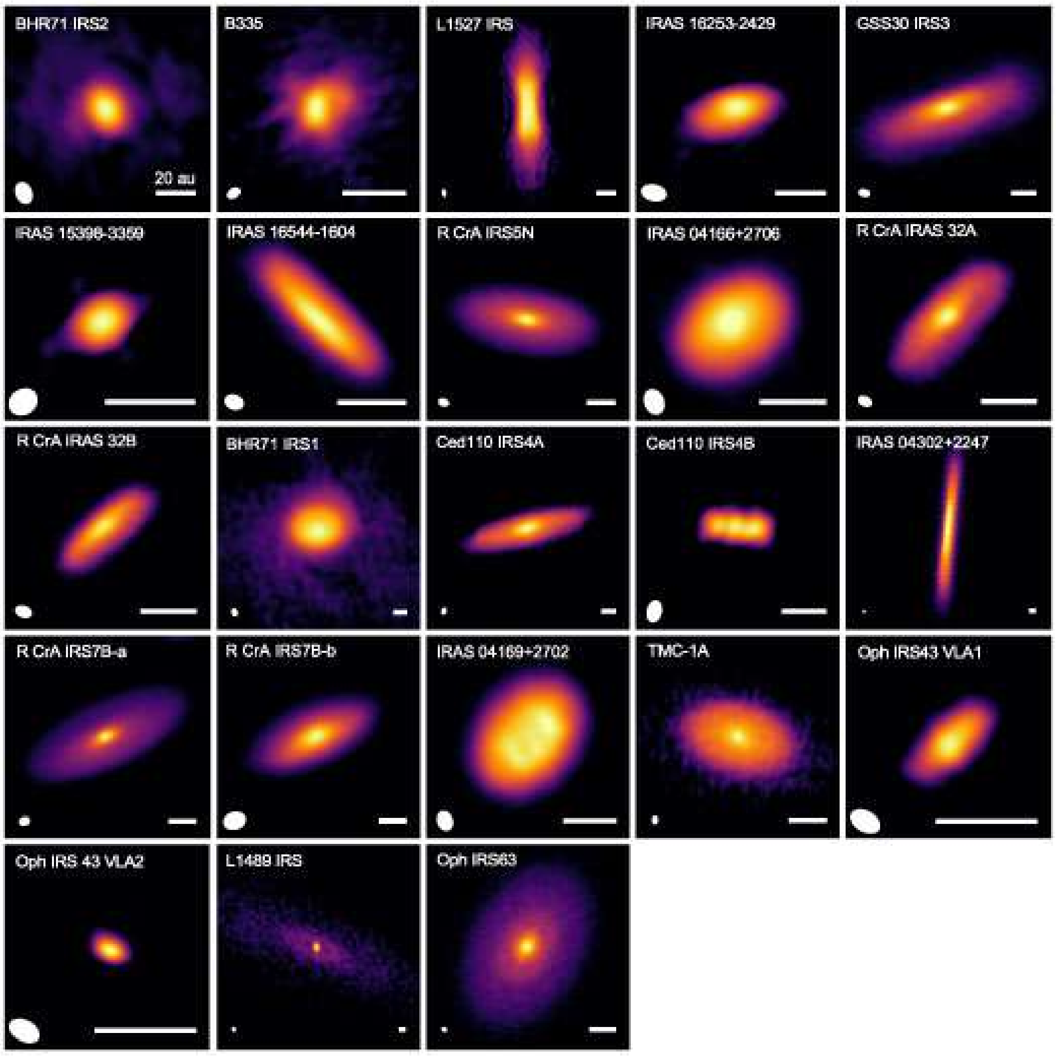

Figure 2. The observation results of protoplanetary disks performed by the edisk project.

to perform long-term calculations including the detailed dust growth and the disk temperature evolution.

To study long-term disk evolution, radially one-dimensional calculations are often used (Nakamoto & Nakagawa 1994; Hueso & Guillot 2005; Zhu et al. 2010; Bae et al. 2013). During the disk formation stage, the infall rate onto the disk is calculated by considering the conservation of angular momentum of the infalling gas within the molecular cloud core (Cassen & Moosman 1981). Takahashi et al. (2013) performed one-dimensional disk calculations employing an analytical model for accretion onto the disk. They demonstrated that their one-dimensional calculation is in good agreement with the results of three-dimensional hydrodynamic simulations. Thus, the one-dimensional calculations are a useful tool for investigating long-term disk evolution. However, it should be noted that many of the one-dimensional calculations did not include a disk wind (outflow) seen in three-dimensional simulations.

Disk winds (outflows) are considered important in disk evolution as they remove mass and angular momentum from the disk. Since the 2010s, one-dimensional calculations for disk evolution considering disk winds have been performed (Suzuki et al. 2016; Bai 2016; Tabone et al. 2022). Takahashi & Muto (2018) calculated the disk evolution of gas and dust, including a disk wind. Their results showed that the disk gas decreases from the inner disk region due to the disk wind, leading to the accumulation of dust in regions with pressure maxima and the formation of ring structures. While their study demonstrated the importance of disk winds in the disk evolution of gas and dust, it has several limitations. For instance, their calculations did not consider the dust growth, disk winds are not driven while the infall onto the disk continues, the removal of angular momentum from the disk by disk winds is not considered, and the disk temperature profile is fixed. These limitations are crucial for considering more realistic disk evolution. Thus, the improvement of these limitations is one of the motivations for this study.

Many studies on dust growth in disks assume evolved Class II isolated disks (Brauer et al. 2008). Recently, calculations considering dust growth in disks assuming Class 0 disks have been performed. Tsukamoto et al. (2017) calculated the dust growth and spatial distribution evolution of dust in Class 0 disks, assuming icy dust particles. For regions inside 10 au, dust particles grow to meter-sized particles, leading to a decrease in dust surface density due to the radial drift. Xu & Armitage (2023) performed calculations on dust evolution assuming rocky dust particles, demonstrating that growth to centimeter-sized particles is possible across the entire disk. These calculations in Class 0 disks for dust growth assumed a steady state for the gas. Some studies have investigated the evolution of dust particles in an evolving disk considering the mass accretion from the envelope onto the disk (Birnstiel et al. 2010; Homma & Nakamoto 2018). However, these studies did not consider the disk wind. The evolution of dust growth and spatial distribution in the evolving disk considering the disk wind remains unclear. Therefore, in this study, we perform one-dimensional disk evolution calculations considering disk wind to investigate its effects on disk structure and dust growth.

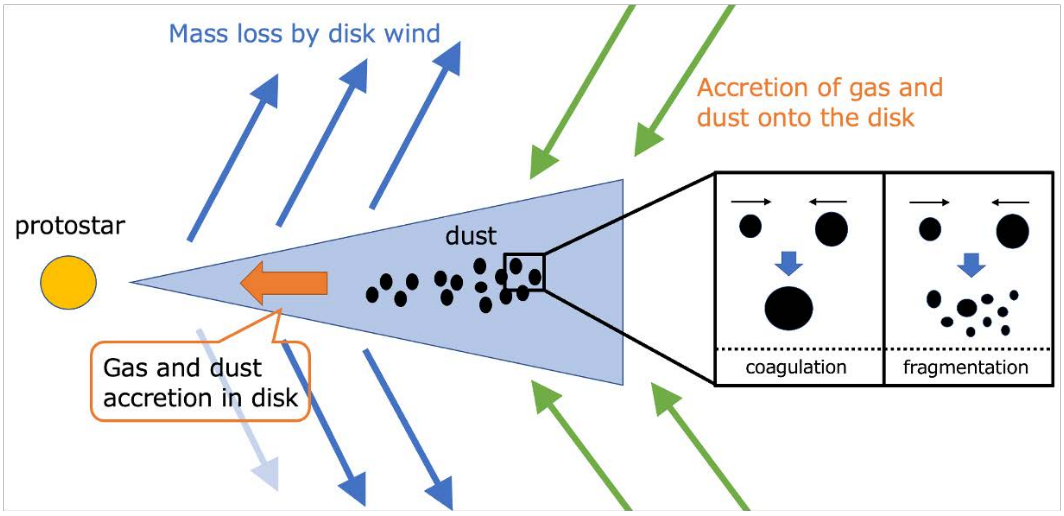

Figure 3. Schematic view of the disk evolution in this study.

2 Methods

In this section, I describe a one-dimensional disk evolution model used in the radial direction to investigate the long-term evolution of a disk. Figure 3 shows the schematic view of disk evolution in this study. I calculate the evolution of the disk from the formation stage. In most one-dimensional disk calculations of previous studies, the rate of mass supply to the disk is obtained analytically from the conservation of angular momentum of the infalling material Cassen & Moosman (1981). In this study, I use the method proposed by Takahashi et al. (2013) to calculate the increase rate of disk surface density by mass supply from the envelope to the disk. Besides the infalling material from the envelope to the disk, I consider mass loss due to disk wind. Recent one-dimensional disk evolution calculations have taken into account magnetically driven disk wind (Suzuki et al. 2016; Bai 2016). In this study, I incorporate the effect of disk wind into disk evolution by using the model from which Tabone et al. (2022) derived the rate of mass loss due to disk wind from the conservation of angular momentum. Within the disk, gas and dust accrete to the center due to viscous or disk wind torque. We consider self-gravitational instability (GI) and magnetorotational instability (Balbus & Hawley (1992);MRI) as the source of the viscosity. The disk wind torque is calculated using the model of Tabone et al. (2022) as well as the mass loss rate. The dust size distribution in the disk changes due to collisional coagulation or fragmentation.

The surface density of gas and dust is defined as follows. The gas surface density is given by

$$\Sigma_{\rm g} = \int \rho_{\rm g} {\rm d}z \tag{2}$$

where $\rho_{\rm g}$ is gas mass density. The dust number density $n_{\rm d}\,(m)$ for a dust mass m is defined as,

$$n_{\rm d}\,(m) \equiv \frac{{\rm d}n_{\rm d}}{{\rm d}m}. \tag{3}$$

Note that the dust number density contained in the dust mass range of m to $m + {\rm d}m$ is

$$n_{\rm d}\,(m)\,{\rm d}m = \frac{{\rm d}n_{\rm d}}{{\rm d}m}{\rm d}m. \tag{4}$$

Using the dust number density, the dust mass density for a dust mass m, $\rho_{\rm d}\,(m)$, is described as

$$\rho_{\rm d}\,(m) = mn_{\rm d}\,(m) = m\frac{{\rm d}n_{\rm d}}{{\rm d}m}. \tag{5}$$

Thus, the dust surface density of mass m is defined as

$$\Sigma_{\rm d}\,(m) \equiv \frac{{\rm d}\Sigma_{\rm d}\,(m)}{{\rm d}m} = \int \rho_{\rm d}\,(m)\,{\rm d}z = \int mn_{\rm d}\,(m)\,{\rm d}z. \tag{6}$$

Also, the vertically integrated number density of dust with mass m is given by

$$N_{\rm d}\,(m) = \int n_{\rm d}\,(m)\,{\rm d}z. \tag{7}$$

In this study, each dust particle is assumed to be compact and spherical, while actual dust particles may be distorted or have porosity. Thus, dust mass with size a is described as $m = (4\pi/3)\rho_{\rm di}a^3$ where $\rho_{\rm di}$ is the internal (material) density of dust particles. It is noted that dust porosity is important for not only dust growth but also dust motion in disks (Ormel et al. 2007; Okuzumi et al. 2012; Kataoka et al. 2013).

2.1 Disk evolution and basic equations

In this sub-section, I present the equations of the gas and dust surface density evolution. Formulas used in this study are based on Takahashi & Muto (2018), and we have extended their formulas. While Takahashi & Muto (2018) treated dust as a single fluid, in this study, we treat dust as a multi-fluid, considering each size separately. The evolutions of the surface density of gas and dust are described by the following equations,

$$\frac{\partial \Sigma_{\rm g}}{\partial t} + \frac{1}{r}\frac{\partial}{\partial r}\left(r\Sigma_{\rm g}v_{{\rm g},r}\right) = \dot{\Sigma}_{\rm g,inf} - \dot{\Sigma}_{\rm g,wind} \tag{8}$$

$$
\begin{aligned}
\frac{\partial \Sigma_{\mathrm{d}}(m)}{\partial t} &+ \frac{1}{r}\frac{\partial}{\partial r}\left[r\Sigma_{\mathrm{d}}(m)\, v_{\mathrm{d},r}(m)\right] \\
&= \frac{1}{r}\frac{\partial}{\partial r}\left[rD_{\mathrm{d}}(m)\,\Sigma_{\mathrm{g}}\frac{\partial}{\partial r}\left(\frac{\Sigma_{\mathrm{d}}(m)}{\Sigma_{\mathrm{g}}}\right)\right] \\
&+ \dot{\Sigma}_{\mathrm{d,inf}}(m) - \dot{\Sigma}_{\mathrm{d,wind}}(m) + \left(\frac{\partial \Sigma_{\mathrm{d}}(m)}{\partial t}\right)_{\mathrm{coag/frag}}, \qquad (9)
\end{aligned}
$$

where $v_{\mathrm{g},r}$ is the gas radial velocity, $v_{\mathrm{d},r}(m)$ is the dust radial velocity, and $\dot{\Sigma}_{\mathrm{g,inf}}$, $\dot{\Sigma}_{\mathrm{g,wind}}$, $\dot{\Sigma}_{\mathrm{d,inf}}$ and $\dot{\Sigma}_{\mathrm{d,wind}}$ represent the mass supply from the infalling envelope onto the disk and the mass loss by the disk wind from the disk of gas and dust, respectively (for details, see §2.4). The second term of the right-hand side of the equation (9) is the turbulent diffusion of dust in a radial direction and D_{d} is the dust turbulent diffusion coefficient. The last term of the right-hand side of the equation (9) represents the mass change rate of dust mass m due to coagulation or fragmentation caused by dust collisions (for details, see §2.5).

The gas and dust velocity is obtained by solving the equations of motion in the radial and azimuthal directions. The radial and azimuthal velocities of the dust $v_{\mathrm{d},r}$ and $v_{\mathrm{d},\phi}$, respectively, are given by

$$
v_{\mathrm{d},r}(m) = \frac{(1+A\mathrm{St}^2)v_{\mathrm{g},r} + 2\mathrm{St}\delta v_{\mathrm{g},\phi} - \mathrm{St}^2\frac{r\dot{M}_{r,\mathrm{tot}}}{M_r}}{1+(1+A)\,\mathrm{St}^2}, \qquad (10)
$$

$$
\delta v_{\mathrm{d},\phi}(m) = \frac{-\mathrm{St}v_{\mathrm{g},r} + 2\delta v_{\mathrm{g},\phi} - \mathrm{St}\frac{r\dot{M}_{r,\mathrm{tot}}}{M_r}}{2\left\{1+(1+A)\,\mathrm{St}^2\right\}}. \qquad (11)
$$

where the dust azimuthal velocity is described by the deviation from the mean azimuthal flow, $\delta v_{\mathrm{d}(m),\phi} = v_{\mathrm{d},\phi}(m) - r\Omega$. The same description is used for the gas azimuthal velocity, $\delta v_{\mathrm{g},\phi} = v_{\mathrm{g},\phi} - r\Omega$. Ω is the angular velocity $\Omega = \left(GM_r/r^3\right)^{1/2}$ and I estimate Ω using enclosed mass M_r within radius r,

$$
M_r = M_* + \int \Sigma_{\mathrm{g}} 2\pi r \mathrm{d}r. \qquad (12)
$$

where M_* is the central stellar mass. $\dot{M}_{r,\mathrm{tot}}$ represents the net disk mass change rate due to the mass supply from the envelope and the mass loss by the disk wind and is described by

$$
\dot{M}_{r,\mathrm{tot}} = \int_0^r 2\pi r\left(\dot{\Sigma}_{\mathrm{g,inf}} - \dot{\Sigma}_{\mathrm{g,wind}}\right)\mathrm{d}r. \qquad (13)
$$

The factor of A represents the effect of the self-gravity of the disk and is described by

$$
A = \frac{2\pi r^2 \Sigma_{\mathrm{g}}}{M_r}. \qquad (14)
$$

Note that I ignore the contribution of dust to equations (12) – (14) because the dust mass is sufficiently smaller than the gas mass.

The Stokes number St is a dimensionless stopping time and is a quantity that indicates the degree of coupling between gas and dust. In a protoplanetary disk, the Stokes number is defined as

$$\mathrm{St} = t_{\mathrm{s}}\Omega, \tag{15}$$

where t_{s} is the stopping time,

$$t_{\mathrm{s}} = \begin{cases} \dfrac{\rho_{\mathrm{di}} a}{\rho_{\mathrm{g}} v_{\mathrm{th}}} & \left(a < \dfrac{9}{4}\lambda_{\mathrm{mfp}}\right) \\ \dfrac{4\rho_{\mathrm{di}} a}{9\rho_{\mathrm{g}} v_{\mathrm{th}} \lambda_{\mathrm{mfp}}} & \left(a > \dfrac{9}{4}\lambda_{\mathrm{mfp}}\right) \end{cases} \tag{16}$$

with ρ_{g} the gas mass density, $v_{\mathrm{th}} = \sqrt{8/\pi} c_s$ the thermal velocity, c_s is the sound speed, λ_{mfp} the gas mean free path, and ρ_{di} the dust internal (material) density. The gas mean free path is described as $\lambda_{\mathrm{mfp}} = m_{\mathrm{g}}/(\sigma_{\mathrm{mol}}\rho_{\mathrm{g}})$, where m_{g} is the gas-particle mass and $\sigma_{\mathrm{mol}} = 2 \times 10^{15}$ cm^2 is the gas molecular cross section. Assuming the gas hydrostatic equilibrium in the vertical direction, one can describe the Stokes number as (Sato et al. 2016)

$$\mathrm{St} = \frac{\pi \rho_{\mathrm{di}} a}{2\Sigma_{\mathrm{g}}} \max\left(1, \frac{4a}{9\lambda_{\mathrm{mfp}}}\right). \tag{17}$$

Additionally, the turbulent diffusion coefficient is given by (Youdin & Lithwick 2007)

$$D_{\mathrm{d}} = \frac{\alpha_{\mathrm{turb}} c_s h_{\mathrm{g}}}{1 + \mathrm{St}^2}. \tag{18}$$

where h_{g} is the gas scale height and α_{turb} is the strength of the turbulence.

The radial and azimuthal velocities of the gas $v_{\mathrm{g},r}$ and $\delta v_{\mathrm{g},\phi}$, respectively, are given by

$$v_{\mathrm{g},r} = \frac{\frac{2r}{j} N (1 + \lambda_2) + 2\lambda_1 (1 + A) r\Omega\eta}{(1 + \lambda_2)^2 + \lambda_1^2 (1 + A)} - \frac{r \dot{M}_{r,\mathrm{tot}}}{M_r}, \tag{19}$$

$$\delta v_{\mathrm{g},\phi} = \frac{\frac{2r}{j} N\lambda_1 - 2(1 + \lambda_2) r\Omega\eta}{2\left\{(1 + \lambda_2)^2 + \lambda_1^2 (1 + A)\right\}}. \tag{20}$$

where η represents the effect of the pressure gradient force and we estimate as,

$$\eta = -\frac{1}{2}\left(\frac{c_s}{r\Omega}\right)^2 \frac{\partial \ln p}{\partial \ln r}, \tag{21}$$

with p the gas pressure at the disk midplane. The λ_1 and λ_2 are quantities related to the dust-to-gas back-reaction and are given by

$$\lambda_1 = \int \frac{\mathrm{St}(m)}{1 + (1 + A)\,\mathrm{St}(m)^2} \epsilon(m)\, \mathrm{d}m \tag{22}$$

$$\lambda_2 = \int \frac{1}{1 + (1 + A)\,\mathrm{St}\,(m)^2} \epsilon\,(m)\,\mathrm{d}m \tag{23}$$

where $\epsilon\,(m)$ represents the dust-to-gas mass ratio of dust mass m,

$$\epsilon\,(m) = \frac{\Sigma_\mathrm{d}\,(m)}{\Sigma_\mathrm{g}}. \tag{24}$$

The specific torque acting on the disk N is described by

$$N = -\frac{1}{r\Sigma_\mathrm{g}} \frac{\partial}{\partial r} \left(\frac{3}{2} r^2 \Sigma_\mathrm{g} \alpha_\mathrm{SS} c_s^2 \right) - \frac{3}{4} \alpha_\mathrm{DW} c_s^2. \tag{25}$$

The first term of equation (25) corresponds to the viscous torque. The Shakura-Sunyaev alpha parameter α_SS (Shakura & Sunyaev 1973) represents the efficiency of angular momentum transport. I consider both self-gravitational instability (GI) and magnetorotational instability (MRI) as the source of the effective viscosity, expressed as

$$\alpha_\mathrm{SS} = \alpha_\mathrm{GI} + \alpha_\mathrm{MRI}, \tag{26}$$

where α_GI and α_MRI are GI and MRI viscous parameter, respectively. In this study, I estimate α_GI as a function of Toomre Q parameter (Zhu et al. 2010),

$$\alpha_\mathrm{GI} = \exp\left(-Q^4\right), \tag{27}$$

where Q is described by

$$Q = \frac{c_s \Omega}{\pi G \Sigma_\mathrm{g}}. \tag{28}$$

This GI viscosity α_GI successfully models a disk evolution due to angular momentum transport by spiral arms in a gravitationally unstable disk as seen in multidimensional numerical simulations (Takahashi et al. 2013).

The MRI activity depends on the ionization state of the gas disk (Gammie 1996; Glassgold et al. 1997; Igea & Glassgold 1999; Bai 2011). Regions where thermal ionization is not effective due to low temperature are magnetically inactive (dead zones), because non-ideal magnetohydrodynamic effects suppress the development of MRI (Sano et al. 2000; Wardle & Salmeron 2012; Kawasaki et al. 2021). The ideal magnetohydrodynamic approximation holds in regions where thermal ionization occurs at high temperature, and MRI becomes active (Desch & Turner 2015). In this study, I use the following expression for α_MRI, which is a function of the midplane temperature (Flock et al. 2016; Ueda et al. 2019).

$$\alpha_\mathrm{MRI} = \frac{\alpha_\mathrm{active} - \alpha_\mathrm{dead}}{2} \left[1 - \tanh\left(\frac{T_\mathrm{MRI} - T}{50\ \mathrm{K}} \right) \right] + \alpha_\mathrm{dead} \tag{29}$$

where $T_\mathrm{MRI} = 1000$ K is a critical temperature above which MRI becomes active (Desch & Turner 2015), $\alpha_\mathrm{active} = 10^{-2}$ is the MRI strength (or viscous parameter) in the MRI active region and $\alpha_{\rm dead} = 10^{-4}$ is that in the MRI inactive region. These MRI related values are fixed in this study. In this study, it is assumed that gravitational instability contributes only to angular momentum transport. In other words, gravitational instability does not contribute to the turbulence strength $\alpha_{\rm turb}$; only MRI is considered to contribute, $\alpha_{\rm turb} = \alpha_{\rm MRI}$. This turbulent strength contributes to the turbulent diffusion of dust particles and the collisional velocity between dust particles.

The second term of the right-hand side in equation (25) is the wind torque term. When disk wind is present, the angular momentum of the gas in the disk should be removed. Thus, the disk gas accretes to the center due to the wind torque. The dimensionless parameter $\alpha_{\rm DW}$ represents the wind torque strength normalized by the thermal pressure in the mid-plane (see Tabone et al. (2022)). In this study, for simplicity, I adopt a constant value of $\alpha_{\rm DW} = 10^{-2}$ in time and space.

2.2 Vertical disk structure of gas and dust

In this study, I assume that the disk gas is in hydrostatic equilibrium in the vertical direction. The gas mass density in the disk given by

$$\rho_{\rm g}\left(z\right) = \frac{\Sigma_{\rm g}}{\sqrt{2\pi}h_{\rm g}} \exp\left(-\frac{z^2}{2h_{\rm g}^2}\right). \tag{30}$$

and gas scale height is described by

$$h_{\rm g} = \frac{c_s}{\Omega}. \tag{31}$$

The vertical structure of the dust is obtained from the equilibrium between the settling to the equatorial plane and turbulent diffusion and is given by (Youdin & Lithwick 2007)

$$\rho_{\rm d}\left(m\right) = \frac{\Sigma_{\rm d}\left(m\right)}{\sqrt{2\pi}h_{\rm d}\left(m\right)} \exp\left[-\frac{z^2}{2h_{\rm d}\left(m\right)^2}\right] \tag{32}$$

The dust scale height is given by

$$h_{\rm d}\left(m\right) = h_{\rm g}\left(1 + \frac{\rm St}{\alpha_{\rm turb}}\frac{1+2{\rm St}}{1+{\rm St}}\right)^{-1/2}. \tag{33}$$

2.3 Energy equation

To obtain the disk midplane temperature, we solve the energy equation as

$$\frac{\partial E}{\partial t} + \frac{1}{r}\frac{\partial}{\partial r}\left(E v_{{\rm g},r}\right) = -\frac{P}{r}\frac{\partial \left(r v_{{\rm g},r}\right)}{\partial r} + Q_{\rm vis} + Q_{\rm shock} + Q_{\rm irr} - \Lambda_{\rm rad} \tag{34}$$

where E is the vertically integrated thermal energy per area,

$$E = \frac{P}{\gamma - 1} = \frac{k_B T}{\mu m_{\rm H} (\gamma - 1)} \Sigma_{\rm g}, \tag{35}$$

in which γ is the specific heat ratio, k_B is the Boltzmann constant, μ is the mean molecular weight, and $m_{\rm H}$ is the hydrogen mass. Although the properties of the gas vary with temperature, we adopt constant values of $\gamma = 7/5$ and $\mu = 2.34$. The vertically integrated pressure P is described by $P = \Sigma_{\rm g} c_s^2$. The heating ($Q_{\rm vis}$, $Q_{\rm shock}$, and $Q_{\rm irr}$) and cooling ($\Lambda_{\rm rad}$) terms are described in the following paragraph.

The heating and cooling rates are adopted based on Nakamoto & Nakagawa (1994). The viscous heating is described by

$$Q_{\rm vis} = -\frac{3}{2} \Sigma_{\rm g} \alpha_{\rm SS} c_s^2 r \frac{\partial \Omega}{\partial r} \tag{36}$$

The shock heating due to infalling gas is described by

$$Q_{\rm shock} = \frac{4\tau + 1}{3\tau^2 + 1} \frac{1}{2} \dot{\Sigma}_{\rm inf} (r\Omega)^2 , \tag{37}$$

where τ is the optical depth, which is calculated as $\tau = \kappa_R \Sigma_{\rm g}/2$ with the Rosseland mean opacity κ_R. The irradiation heating is given by

$$Q_{\rm irr} = \frac{8\tau}{3\tau^2 + 1} \sigma_{\rm SB} \left(T_{\rm irr}^4 + T_{\rm amb}^4 \right) , \tag{38}$$

where $T_{\rm amb} = 10$ K is the temperature of ambient gas in a collapsing cloud core. The irradiation flux $\sigma_{\rm SB} T_{\rm irr}^4$ is due to the central star and is represented as (Ruden & Pollack 1991)

$$\sigma_{\rm SB} T_{\rm irr}^4 = \frac{L_\star + L_{\rm acc}}{4\pi r^2} \left[\frac{2}{3\pi} \frac{R_\star}{r} + \frac{1}{2} \frac{h_{\rm g}}{r} \left(\frac{{\rm d} \ln h_{\rm g}}{{\rm d} \ln r} - 1 \right) \right] , \tag{39}$$

where $\sigma_{\rm SB}$ is the Stefan–Boltzmann constant, the term $({\rm d} \ln H / {\rm d} \ln r - 1)$ is the shielding factor, $L_\star$ is the stellar luminosity, and $L_{\rm acc}$ is the accretion luminosity. To avoid numerical instabilities, we set the shielding factor to be constant ${\rm d} \ln h_{\rm g} / {\rm d} \ln r = 9/7$ (Hueso & Guillot 2005). I calculate $L_\star$ by the following mass–luminosity relation (Bae et al. 2013).

$$\log_{10} \left(\frac{L_\star}{L_\odot} \right) = 0.2 + 1.74 \log_{10} \left(\frac{M_\star}{M_\odot} \right) . \tag{40}$$

The accretion luminosity $L_{\rm acc}$ is estimated as

$$L_{\rm acc} = \frac{G M_\star \dot{M}}{2 R_\star}, \tag{41}$$

where we assume a central star radius of $R_\star = 2 R_\odot$.

The radiative cooling rate is described by

$$\Lambda_{\rm rad} = \frac{8\tau}{3\tau^2 + 1} \sigma_{\rm SB} T^4 . \tag{42}$$

The opacity value is taken from Zhu et al. (2012). Figure 4 shows the opacity against temperature in the case of assuming the gas mass density $\rho_{\rm g} = 10^{-10}$ g cm^{-3}.

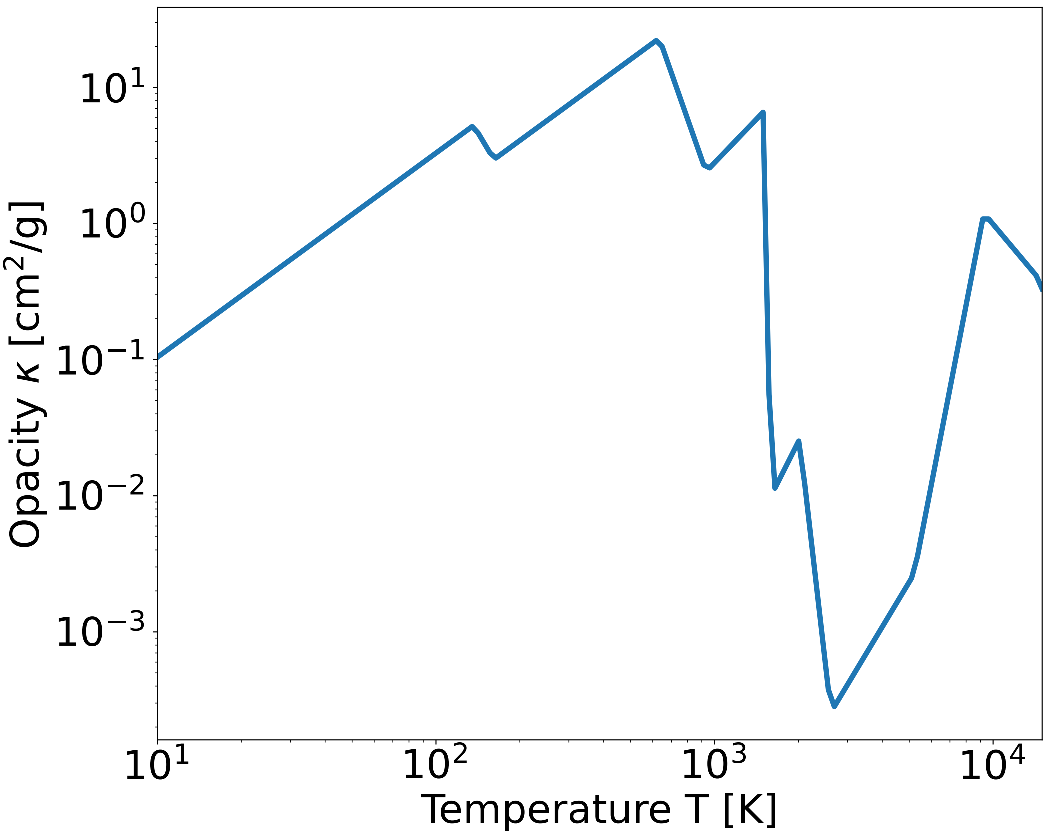

Figure 4. The opacity against temperature in the case of assuming the gas mass density $\rho_g = 10^{-10}$ g cm^{-3}.

2.4 Infall and disk wind models

To obtain the rate of increase of the disk surface density due to mass infall from the cloud core $\dot{\Sigma}_{\rm inf}$, we use a model proposed by Takahashi et al. (2013). As the initial state of the core, I consider a critical Bonner–Ebert (B.E.) density profile (Ebert 1955; Bonnor 1956). I then increase the density by a factor f so that the gravitational force is stronger than the pressure gradient force (Machida et al. 2006). For the B.E. core, the time for the spherical shell initially at position $R_{\rm ini}$ to reach the central region is given by

$$t_{\rm inf} = \frac{2}{\pi} t_{\rm ff} \int_0^1 \frac{{\rm d}x}{\sqrt{f^{-1} \ln x + x^{-1} - 1}} \tag{43}$$

where $t_{\rm tff}$ is the free-fall time. The free fall time of the cloud shell initially at $R_{\rm ini}$ is estimated as

$$t_{\rm rff} = \frac{\pi}{2} \sqrt{\frac{R_{\rm ini}^3}{2GM(R_{\rm ini})}} \tag{44}$$

where $M(R_{\rm ini})$ is the mass within radius $R_{\rm ini}$. Using $t_{\rm inf}$, the mass accretion rate onto the disk and star is described by

$$\dot{M}_{\rm inf}(t) = 4\pi R_{\rm ini}^2 \rho_{\rm ini}(R_{\rm ini}) \left(\left. \frac{\mathrm{d}t_{\rm inf}}{\mathrm{d}R_{\rm ini}} \right|_{t_{\rm inf}=t} \right)^{-1}, \tag{45}$$

where $\rho_{\rm ini}(R_{\rm ini})$ is the initial density of the B.E. core at radius $R_{\rm ini}$.

I assume that the core rigidly rotates with angular velocity $\Omega_{\rm core}$ and the specific angular momentum of the infalling gas during collapse is conserved. Assuming that the cloud gas accretes at the centrifugal radius, the mass infall rate at each radius r is described by

$$\dot{\Sigma}_{\rm inf} = \frac{1}{2\pi r} \frac{\dot{M}_{\rm inf}}{2\Omega_{\rm core} R_{\rm ini}^2} \left(1 - \frac{j}{\Omega_{\rm core} R_{\rm ini}^2} \right)^{-1/2} \frac{\partial j}{\partial r}, \tag{46}$$

The cloud collapse and accretion models adopted in this study agree well with the three-dimensional hydrodynamic simulations (Machida et al. 2010; Takahashi et al. 2013). I regard $\dot{\Sigma}_{\rm inf}$ as the sum of the mass increase rate of the disk of gas and dust. In this study, I assume that the dust-gas-mass ratio in the molecular cloud core is $f_{\rm dg} = 0.01$ and the infalling dust size is $a_0 = 0.1\ \mu$ m. Then, the mass infall rates into the disk of gas and dust are described as, respectively,

$$\dot{\Sigma}_{\rm g,inf} = (1 - f_{\rm dg})\dot{\Sigma}_{\rm inf}, \tag{47}$$

$$\dot{\Sigma}_{\rm d,inf}(m) = f_{\rm dg}\dot{\Sigma}_{\rm inf}\delta(m - m_0). \tag{48}$$

where m_0 is the dust mass with radius a_0 and $\delta(x)$ is the Dirac delta function.

For the mass loss rate due to the disk wind, we use a model adopted in Tabone et al. (2022):

$$\dot{\Sigma}_{\rm g,wind} = \frac{3\alpha_{\rm DW}\Sigma_{\rm g} c_s^2}{4j(\lambda - 1)}, \tag{49}$$

where $j = r^2\Omega$ is the specific angular momentum in a disk and λ is the parameter of the magnetic lever arm. This formula is obtained from the angular momentum conversation of the disk wind. The extent to which dust particle of a certain size is blown away by the disk wind is not well understood. In this study, it is assumed that dust particle with a Stokes number less than 10^{-4} is removed by the disk wind. The mass loss rate of dust particles with mass m due to the disk wind is assumed to be given by

$$\dot{\Sigma}_{\rm d,wind}(m) = \frac{3\alpha_{\rm DW}\Sigma_{\rm d}(m) c_s^2}{4j(\lambda - 1)}. \tag{50}$$

As described above, I consider both mass gain into the disk and mass loss from the disk. Thus, I need to determine what mass gain or mass loss occurs at each radius of the disk. The mass gain is attributed to gas inflow from the infalling envelope, while the mass loss is attributed to the disk wind.

The wind driving condition depends on the strength of the magnetic field and the surrounding gas density (Machida & Hosokawa 2020). In this study, I compare the ram pressure of the infalling gas with that of the outflowing gas. The velocity of the gas infalling to the central region is estimated to be $v_{\rm inf} \sim \sqrt{GM_r/r}$. On the other hand, assuming that the energy source of the wind drive is gravitational energy, the velocity of the wind is also described by $v_{\rm wind} \sim \sqrt{GM_r/r}$ (e.g., Kudoh & Shibata 1997). Since $v_{\rm inf}$ and $v_{\rm wind}$ are similar in magnitude, the densities of the infalling and outflowing gas determine whether the ram pressure of the infalling or outflowing gas is greater. Thus, by comparing the infall rate $\dot{\Sigma}_{\rm inf}$ and the mass loss rate $\dot{\Sigma}_{\rm wind}$, we can determine whether mass infall into the disk or mass loss from the disk occurs. When $\dot{\Sigma}_{\rm inf} > \dot{\Sigma}_{\rm wind}$, the infall occurs without driving wind and we set $\dot{\Sigma}_{\rm wind} = 0$, and vice versa.

2.5 Evolution of dust size evolution

2.5.1 Coagulation and fragmentation equation

The size of dust particles changes due to coagulation and fragmentation caused by the collision of dust particles. The time evolution of the surface density of dust with mass m within the disk due to coagulation and fragmentation is described by the following equation (Smoluchowski 1916),

$$\begin{aligned}\left(\frac{\partial \Sigma_{\rm d}(m)}{\partial t}\right)_{\rm coag/frag} =& \frac{1}{2}\int_0^m m\tilde{K}(m-m',m)\,N_{\rm d}(m-m')\,N_{\rm d}(m')\,{\rm d}m' \\ &- \int_0^\infty \tilde{K}(m,m')\,N_{\rm d}(m)\,N_{\rm d}(m') \\ &+ \frac{1}{2}\int\int_0^\infty m\tilde{F}(m_1,m_2)\,N_{\rm d}(m_1)\,N_{\rm d}(m_1)\,\varphi_{\rm f}(m;m_1,m_2)\,{\rm d}m_1{\rm d}m_2 \\ &- \int_0^\infty m\tilde{F}(m,m_1)\,N_{\rm d}(m)\,N_{\rm d}(m_1)\,{\rm d}m_1 \end{aligned} \tag{51}$$

where $N_{\rm d}(m)$ is the vertically integrated number density of dust mass m, $\tilde{K}$ and $\tilde{F}$ are the vertical integrated coagulation and fragmentation kernels, $\varphi_f(m;m_1,m_2)$ is the distribution function for fragments after a collision between m_1 and m_2 dust particles. The kernels $\tilde{K}$ and $\tilde{F}$ are given by (Stammler & Birnstiel 2022)

$$\tilde{K}(m,m') = \frac{K(m,m')}{\sqrt{2\pi\left[h_d(m)^2 + h_d(m')^2\right]}}, \tag{52}$$

$$\tilde{F}(m,m') = \frac{F(m,m')}{\sqrt{2\pi\left[h_d(m)^2 + h_d(m')^2\right]}} \tag{53}$$

where K and F are the coagulation and fragmentation kernels and described in 2.5.3.

The first two terms on the right-hand side of Eq. (51) correspond to an increase or decrease in dust density due to coagulation. The next two terms represent an increase or decrease in dust density due to fragmentation.

2.5.2 Relative velocity between dust particles

The relative velocity among dust particles is an important factor in determining the collision rate and the outcome of dust collisions. As the origin of the relative velocity between dust particles, we consider turbulence, thermal motion (or Brownian motion), radial drift, azimuthal drift, and vertical settling.

I adopt the model presented by Ormel & Cuzzi (2007) to calculate the relative velocities between dust particles induced by turbulence. The relative velocity due to two dust particles, mass m_1 and m_2, is given by the following equations:

$$\Delta v_{\rm turb} = \sqrt{\Delta v_{\rm I}^2 + \Delta v_{\rm II}^2}, \tag{54}$$

$$\begin{aligned}\Delta v_{\rm I}^2 = &\sqrt{\frac{3}{2}} v_{\rm turb} \frac{\mathrm{St}_1 - \mathrm{St}_2}{\mathrm{St}_1 + \mathrm{St}_2} \\ &\times \left(\frac{\mathrm{St}_1^2}{\mathrm{St}_{1,2}^* + \mathrm{St}_1} - \frac{\mathrm{St}_1^2}{1+\mathrm{St}_1} - \frac{\mathrm{St}_2^2}{\mathrm{St}_{1,2}^* + \mathrm{St}_2} + \frac{\mathrm{St}_2^2}{1+\mathrm{St}_2} \right),\end{aligned} \tag{55}$$

$$\begin{aligned}\Delta v_{\rm II}^2 = &\sqrt{\frac{3}{2}} v_{\rm turb} \left(\mathrm{St}_{1,2}^* - \mathrm{St}_{\rm min}\right) \\ &\times \left\{ \frac{\left(\mathrm{St}_{1,2}^* + \mathrm{St}_{\rm min}\right)\mathrm{St}_1 + \mathrm{St}_{1,2}^*\mathrm{St}_{\rm min}}{\left(\mathrm{St}_1 + \mathrm{St}_{1,2}^*\right)\left(\mathrm{St}_1 + \mathrm{St}_{\rm min}\right)} \right. \\ &\left. + \frac{\left(\mathrm{St}_{1,2}^* + \mathrm{St}_{\rm min}\right)\mathrm{St}_2 + \mathrm{St}_{1,2}^* St_{\rm min}}{\left(\mathrm{St}_2 + \mathrm{St}_{1,2}^*\right)\left(\mathrm{St}_2 + \mathrm{St}_{\rm min}\right)} \right\},\end{aligned} \tag{56}$$

where $v_{\rm turb} = \alpha_{\rm turb} c_s^2$ is the gas turbulent velocity, St_1 and St_2 are the Stokes number of dust mass m_1 and m_2, $\mathrm{St}_{\rm min} = \tau_\eta/\tau_{\rm L} = 1/\sqrt{\mathrm{Re}}$ and $\mathrm{St}_{1,2}^* = \max\left(St_{\rm min}, \min\left(1.6St_1, 1\right)\right)$.

The relative velocity by Brownian motion is given by

$$\Delta v_{\rm br}(m_1, m_2) = \sqrt{\frac{8k_B T\left(m_1 + m_2\right)}{m_1 m_2}}. \tag{57}$$

When the mass or size of the dust particles differs, they have different velocities, resulting in the relative velocity. The relative velocities due to drift motions between dust particles with masses m_1 and m_2 are given by the following equations (Okuzumi et al. 2009; Ohashi et al. 2021; Kobayashi & Tanaka 2021):

$$\Delta v_{\mathrm{d},r}\left(m_1, m_2\right) = \left|v_{\mathrm{d},r}\left(m_1\right) - v_{\mathrm{d},r}\left(m_2\right)\right| \tag{58}$$

$$\Delta v_{\mathrm{d},\phi}\left(m_1, m_2\right) = \left|v_{\mathrm{d},\phi}\left(m_1\right) - v_{\mathrm{d},\phi}\left(m_2\right)\right| \tag{59}$$

$$\Delta v_{\mathrm{d},z}\left(m_1, m_2\right) = \left(\frac{\mathrm{St}_1}{1+\mathrm{St}_1} - \frac{\mathrm{St}_2}{1+\mathrm{St}_2}\right) \frac{h_{\mathrm{d}}\left(m_1\right) h_{\mathrm{d}}\left(m_2\right)}{\sqrt{\pi\left(h_{\mathrm{d}}^2\left(m_1\right) + h_{\mathrm{d}}^2\left(m_2\right)\right)}} r\Omega \tag{60}$$

2.5.3 Coagulation and fragmentation kernels

The outcome of dust collision depends on various factors such as the relative velocity between dust particles, the collision cross-section, and the internal properties of the dust. Although they can all be included in the kernel, it is difficult to deal with all of them, and many studies have simplified the problem. In this study, I use a dust coagulation and fragmentation kernel that takes into account the probabilistic distribution of dust relative velocities (Garaud et al. 2013; Booth et al. 2018). The coagulation K_{ij} and fragmentation F_{ij} kernels of dust particles i and j are described as

$$K_{ij} = s_{ij} \int_0^\infty \Delta v P_{ij}(\Delta v) \epsilon_{ij}^{\mathrm{c}}(\Delta v)\, \mathrm{d}\Delta v, \tag{61}$$

$$F_{ij} = s_{ij} \int_0^\infty \Delta v P_{ij}(\Delta v) \epsilon_{ij}^{\mathrm{f}}(\Delta v)\, \mathrm{d}\Delta v, \tag{62}$$

where s_{ij} is the collision cross section and is estimated as $s_{ij} = \pi\left(a_i + a_j\right)^2$ assuming each dust particle is a sphere with radii a_i and a_j.

$P_{ij}(\Delta v)$ is the probability distribution function for the relative velocity of two dust particles. The collision velocity between dust particles of arbitrary size is assumed to be given by a Gaussian distribution (Windmark et al. 2012b; Stammler & Birnstiel 2022):

$$P_{ij}(\Delta v) = \sqrt{\frac{54}{\pi}} \frac{\Delta v^2}{v_{\mathrm{rel},ij}^3} \exp\left(-\frac{3\Delta v^2}{2 v_{\mathrm{rel},ij}^2}\right), \tag{63}$$

where Δv is the relative velocity of the dust and $v_{\mathrm{rel},ij}$ is the total relative velocity,

$$v_{\mathrm{rel},ij} = \sqrt{\Delta v_{\mathrm{turb},ij}^2 + \Delta v_{\mathrm{br},ij}^2 + \Delta v_{\mathrm{d},r,ij}^2 + \Delta v_{\mathrm{d},\phi,ij}^2 + \Delta v_{\mathrm{d},z,ij}^2} \tag{64}$$

In equations (61) and (62), $\epsilon_{ij}^{c}(\Delta v)$ and $\epsilon_{ij}^{f}(\Delta v)$ represent the probability of coagulation or fragmentation of dust particles after a collision, respectively. These probabilities depend on the collision velocity and the properties of the dust. However, in this study, we simply assume that the dust particles coagulate when the relative velocity between dust particles is $v < v_c$ and fragments when $v > v_f$ (Windmark et al. 2012b). In other words, $\epsilon_{ij}^{c}(\Delta v)$ and $\epsilon_{ij}^{f}(\Delta v)$ are given by a Heaviside step function as follows,

$$\epsilon^{c}(\Delta v) = H(v_c - \Delta v), \tag{65}$$

$$\epsilon^{f}(\Delta v) = H(\Delta v - v_f), \tag{66}$$

where v_c and v_f are introduced in Section 2.5.4.

The coagulation and fragmentation kernels can then be expressed as follows,

$$\begin{aligned} K_{ij} &= s_{ij}\int_0^{\infty} \Delta v P_{ij}(\Delta v)\epsilon^{\mathrm{c}}(\Delta v)\,\mathrm{d}\Delta v \\ &= s_{ij}\int_0^{v_c} \Delta v P_{ij}(\Delta v)\mathrm{d}\Delta v \\ &= s_{ij}\sqrt{\frac{8\pi}{3}}v_{\mathrm{rel},ij}\left[1-\left(1+\frac{3v_f^2}{2v_{\mathrm{rel},ij}^2}\right)\exp\left(-\frac{3v_f^2}{2v_{\mathrm{rel},ij}^2}\right)\right], \end{aligned} \tag{67}$$

$$\begin{aligned} F_{ij} &= s_{ij}\int_0^{\infty} \Delta v P_{ij}(\Delta v)\epsilon^{\mathrm{f}}(\Delta v)\,\mathrm{d}\Delta v \\ &= s_{ij}\int_{v_f}^{\infty} \Delta v P_{ij}(\Delta v)\mathrm{d}\Delta v \\ &= s_{ij}\sqrt{\frac{8\pi}{3}}v_{\mathrm{rel},ij}\left(1+\frac{3v_f^2}{2v_{\mathrm{rel},ij}^2}\right)\exp\left(-\frac{3v_f^2}{2v_{\mathrm{rel},ij}^2}\right). \end{aligned} \tag{68}$$

2.5.4 Fragmentation model

The fragmentation model used in this study is constructed based on numerical dust collision calculations (Wada et al. 2013) and is essentially the same Kawasaki et al. (2022). When dust fragmentation occurs as a result of the collision of two dust particles ($m_1 > m_2$), the fragments obey the following mass distribution function φ_{f},

$$m\varphi_{\mathrm{f}}(m; m_1, m_2) = m_{\mathrm{rm}}\delta(m - m_{\mathrm{m}}) + m g_{\mathrm{f}}(m; m_1, m_2). \tag{69}$$

The first term on the right-hand side represents the dominant mass remaining in the fragments, and the second term represents the continuous distribution of the other masses. The continuous mass distribution function is represented by the power distribution $g_{\mathrm{f}} \propto m^{-\xi}$ in the range ($m_{\mathrm{f,min}} \leqslant m \leqslant m_{\mathrm{f,max}}$). The conservation of mass before and after the collision can be described as

$$m_1 + m_2 = \int_0^{\infty} m\varphi_{\mathrm{f}}(m; m_1, m_2)\,\mathrm{d}m. \tag{70}$$

The normalization constant of g_{f} can be obtained from equation (70), and g_f is

$$g_{\mathrm{f}}\left(m; m_1, m_2\right) = \frac{\left(m_1 + m_2 - m_{\mathrm{rm}}\right)(2-\xi)}{m_{\mathrm{f,max}}^{2-\xi} - m_{\mathrm{f,min}}^{2-\xi}} m^{-\xi}. \tag{71}$$

In this study, I use $\xi = 11/6 = 1.83$ (Brauer et al. 2008; Kobayashi & Tanaka 2010).

We need m_{rm} to determine the mass distribution function. I use the relational equation obtained from numerical dust collision experiments to determine the mass m_{ej} ejected after the two dust particles collide (Wada et al. 2013),

$$m_{\mathrm{ej}} = \frac{v}{v_{\mathrm{col,crit}}} m_2, \tag{72}$$

where v is the collision velocity for dust particles and $v_{\mathrm{col,crit}}$ is the velocity required for most of the dust particles to fragment after the collision. The value of $v_{\mathrm{col,crit}}$ depends on the composition and the structure of dust particles. The typical value of $v_{\mathrm{col,crit}}$ for silicate dust particles has been estimated to be in the range $1 - 10\ \mathrm{m\ s^{-1}}$ through laboratory experiments and numerical simulations. For water-icy dust particles, the typical value of $v_{\mathrm{col,crit}}$ is considered to be higher compared to silicate dust particles. In this study, I assume that in regions with temperatures higher than 160 K, the composition of dust particles is silicate, while in regions with temperatures lower than 160 K, the composition of dust particles is water ice. Although $v_{\mathrm{col,crit}}$ may depend on the mass ratio of colliding dust, for simplicity, we assume it does not depend on the mass ratio and use the following values,

$$v_{\mathrm{col,crit}} = \begin{cases} 1\ \mathrm{m\ s^{-1}} & (T > 160\ \mathrm{K,\ silicate}) \\ 10\ \mathrm{m\ s^{-1}} & (T < 160\ \mathrm{K}\ ,\mathrm{H_2O\ ice}) \end{cases} \tag{73}$$

Thus, m_{rm} is described as

$$m_{\mathrm{rm}} = m_1 + m_2 - m_{\mathrm{ej}}. \tag{74}$$

When the collision velocity v is less than $v_{\mathrm{col,crit}}$, m_{ej} is less than m_2. In this case, m_{rm} is greater than m_1. In other words, the fragmentation model used in this study also includes mass transport between the two colliding dust particles.

The minimum mass $m_{\mathrm{f,min}}$ of the mass distribution function $g_f\left(m; m_1, m_2\right)$ is set to be m_0. The maximum mass $m_{\mathrm{f,max}}$ is set to be $m_{\mathrm{f,max}} = 0.1\, m_{\mathrm{ej}}$. If the collision velocity u is greater than $v_{\mathrm{col,crit}}$, most of the dust particle is destroyed and $m_{\mathrm{f,max}} > m_{\mathrm{rm}}$ is realized. In this case, I do not consider m_{rm} $(= 0)$, and assume that the mass of $m_{\mathrm{ej}} = m_1 + m_2$ is distributed according to the distribution function $g_f\left(m; m_1, m_2\right)$ (eq. 71).

2.6 Dust evaporation and condensation

When the temperature becomes high, dust particles can completely evaporate. In this study, vapor components evaporated from dust particles are treated separately from the disk gas. I assume that the dust particles evaporate when the disk temperature is higher than 1500 K. On the other hand, when the disk temperature decreases from above 1500 K to below, vapor condenses into dust particles. The size of the condensed dust particles is assumed to be $a_0 = 0.1\ \mu$ m. The surface density Σ_v of vapor follows the equation below:

$$\frac{\partial \Sigma_\mathrm{v}}{\partial t} + \frac{1}{r}\frac{\partial}{\partial r}\left[r\Sigma_\mathrm{v} v_{\mathrm{v},r}\right] = \frac{1}{r}\frac{\partial}{\partial r}\left[rD_\mathrm{v}\Sigma_\mathrm{g}\frac{\partial}{\partial r}\left(\frac{\Sigma_\mathrm{v}}{\Sigma_\mathrm{g}}\right)\right] - \dot{\Sigma}_{\mathrm{v,wind}}, \tag{75}$$

where $v_{\mathrm{v},r}$ is the vapor velocity and set to be the same $v_{\mathrm{g},r}$, D_v is the turbulent diffusion coefficient of vapor,

$$D_\mathrm{v} = \alpha_\mathrm{turb} c_s h_\mathrm{g}, \tag{76}$$

and $\dot{\Sigma}_{\mathrm{v,wind}}$ represent the mass loss of vapor due to a disk wind,

$$\dot{\Sigma}_{\mathrm{v,wind}} = \frac{3\alpha_\mathrm{DW}\Sigma_\mathrm{v} c_s^2}{4j\left(\lambda - 1\right)}. \tag{77}$$

2.7 Numerical Settings

I set the computational domain from 0.3 au to 10^3 au and divide the region into 200 logarithmic divisions. I solve the differential equations (8), (9), (34) and (75) explicitly. To solve the coagulation-fragmentation equation (51), I use the bin method as Kawasaki et al. (2021). The computational domain of dust radius is in the range $a = 10^{-5} - 10^{5}$ cm, and this range is derived into uniform logarithmic intervals with a resolution of tens bins per decade. The internal density of dust particles is assumed to be a constant value of $\rho_\mathrm{di} = 2.65$ g cm^{-3} although it depends on the composition and the structure of dust particles. I adopt zero-gradient boundary conditions at the inner boundary and impose the condition that disk material flows out from the boundary only if $v_{\mathrm{g(d),r}} < 0$. I also set the flux at the outer boundary to be zero. The central density and angular velocity of the molecular cloud core are listed in Table 1. I start our calculations with a protostellar mass of 0.01 $M_\odot$ without a disk. I set the end of the calculations to 3×10^5 years. I perform calculations with and without disk wind to investigate the effect of disk wind on disk evolution. In the calculations with disk wind, we set the parameters $\alpha_\mathrm{DW} = 10^{-2}$ and $\lambda = 2$.

Table 1. Parameters used in this study.

$M_{\rm core}$	$1.0\ M_\odot$	total mass of cloud core
$\Omega_{\rm core}$	$2.0 \times 10^{-14}\ {\rm s}^{-1}$	angular velocity of cloud core
$T_{\rm core}$	10 K	temperature of cloud core
n_0	$3 \times 10^5\ {\rm cm}^{-3}$	central density of cloud core
f	1.4	density enhancement factor of cloud core
$T_{\rm MRI}$	1000 K	MRI activate temperature
$\alpha_{\rm dead}$	10^{-4}	alpha parameter for dead zone
$\alpha_{\rm active}$	10^{-2}	alpha parameter for MRI active region
$\alpha_{\rm DW}$	10^{-2}	dimensionless parameter of disk wind
λ	2	magnetic lever arm parameter

3 Results

In this section, I first describe the results of the case without disk wind. Next, I present the results of the case with disk wind. Finally, I compare the results between the cases without and with disk wind.

3.1 Case without disk wind

This subsection described the results of gas disk evolution without disk wind. The top panel of Fig. 5 shows the time evolution of the mass infall rate to the entire star–disk system from the core (or infalling envelope) $\dot{M}_{\rm inf}$ and the mass accretion rate from disk to the central star $\dot{M}_{\rm acc}$. In the case without the disk wind, $\dot{M}_{\rm inf}$ is the same as calculated from equation (45). We define the period during which mass infall from the cloud core (or the infalling envelope) occurs as the infall phase. The infall phase lasts until $t \simeq 1.89 \times 10^5$ year in our setting of the cloud core. The infall rate in this phase is as high as $\dot{M}_{\rm inf} \simeq 10^{-5}$ $\mathrm{M_\odot yr^{-1}}$. After the infall phase ($t \gtrsim 1.89 \times 10^5$ years), the mass infall rate becomes zero because all the initial core mass has reached the central region.

The mass accretion from the disk to star $\dot{M}_{\rm acc,d}$ shows an episodic behavior. I call the local peaks of the mass accretion rate outbursts. During the infall phase, outbursts have a mass accretion rate of $\dot{M}_{\rm acc} \simeq 2 \times 10^{-5}$ $\mathrm{M_\odot}$ $\mathrm{yr^{-1}}$. This accretion rate is larger than the mass infall rate $\dot{M}_{\rm inf}$. After the infall phase ($t \gtrsim 1.89 \times 10^5$ year), the local peak of outbursts gradually decreases and has $\dot{M}_{\rm acc} \simeq 10^{-6}$ $\mathrm{M_\odot yr^{-1}}$

The behavior of the mass accretion rate is similar to the model with non-zero viscosity in the dead zone in Bae et al. (2013, 2014). Bae et al. (2013) refer that accretion bursts are thermally driven when non-zero small viscosity exists in the dead zone. We confirm that outbursts in our calculations are driven by a similar process.

The time interval between outbursts is different between during the infall phase and after the infall phase. During the infall phase, the time interval between the outbursts is about 8×10^3 year. After the infall phase, the time interval between the outbursts is about 2×10^4 year. During the infall phase, for the inner region of the disk, there is not only the mass accretion from the outer disk region but also the infall mass from the cloud core. The viscous heating rate increases as the gas surface density increases. Thus, the time of thermal evolution of the inner disk region is

Table 2. Masses of the protostar, disk, and disk wind at the end of the infall phase and at the end of the calculation.

	End of infall phase			End of calculation		
Runs	$M_{\rm star}\,[M_\odot]$	$M_{\rm disk}\,[M_\odot]$	$M_{\rm wind}\,[M_\odot]$	$M_{\rm star}\,[M_\odot]$	$M_{\rm disk}\,[M_\odot]$	$M_{\rm wind}\,[M_\odot]$
Without disk wind	0.57	0.43	–	0.66	0.34	–
With disk wind	0.31	0.31	0.39	0.34	0.17	0.49

shorter than that of the phase after the infall from the core. As a result, the frequency of the outbursts is high during the infall phase.

The middle panel of Fig. 5 plots the time evolution of masses of the disk and the central star. The masses of the disk and the central star at the end of the infall phase and the end of the calculation are described in Table 2. During the infall phase, the disk and stellar masses increase due to the high mass infall and accretion rates. At the end of the infall phase, the masses of the disk and the central star are $M_{\rm disk} \simeq 0.43\ {\rm M}_\odot$ and $M_\star \simeq 0.57\ {\rm M}_\odot$, respectively. After the infall phase, the disk mass slowly decreases because no mass reservoir exists outside the disk (or no infalling envelope). Thus, no disk mass can be supplied from the infalling envelope. Even after the infall phase, the stellar mass slowly increases due to mass accretion from the disk. At the end of the calculation time (3.0×10^5 years), the disk and stellar masses are $M_{\rm disk} \simeq 0.34\ {\rm M}_\odot$, $M_{\rm star} \simeq 0.66\ {\rm M}_\odot$, respectively.

The bottom panel of Fig. 5 shows the time evolution of the stellar luminosity $L_\star$ and the accretion luminosity $L_{\rm acc}$. The accretion luminosity shows time variations caused by episodic mass accretions. During the infall phase, the accretion luminosity is always higher than the stellar luminosity. After the infall phase, the accretion luminosity decreases as the mass accretion rate to the central star decreases. However, the accretion luminosity at the peak (outburst epoch) is still higher than the stellar internal luminosity after the infall phase.

3.1.1 Gas evolution without disk wind

Figure 6 shows the radial profile of the surface density, temperature, Toomre Q parameter, and viscous alpha parameter $\alpha_{\rm SS}$ at four different epochs during the infall phase in the case without disk wind. In the upper left panel of Fig. 6, the gas surface density is shown as solid lines, dust as dashed lines, and vapor as dotted lines, respectively. In the upper right panel of Fig. 6, I plot a horizontal dashed line where $T = 160$ K. As described in Section 2.5.4, dust particles are regarded as silicate (bear) particles in the disk regions where the temperature is higher than

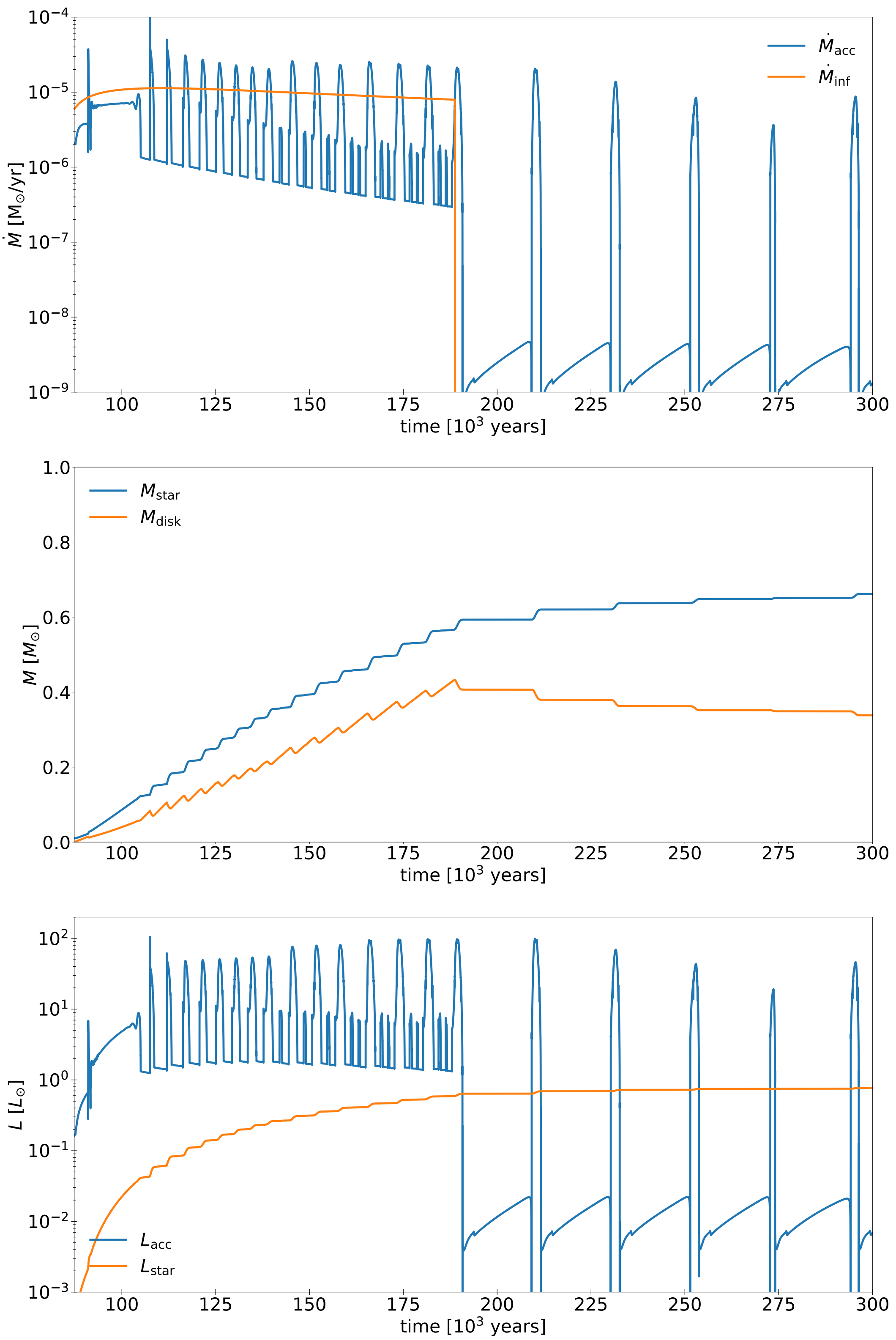

Figure 5. Time evolution of physical quantities in the case without disk wind. (Top) Mass accretion rate from the disk to the star $\dot{M}_{\rm acc}$ and mass infall rate from the infalling envelope to the disk $\dot{M}_{\rm inf}$. (Middle) Disk $M_{\rm disk}$ and central stellar $M_{\rm star}$ masses. (Bottom) Stellar luminosity $L_\star$ and accretion luminosity $L_{\rm acc}$ for the case without disk wind.

160 T. On the other hand, in the disk region where $T > 160$ K, dust particles are regarded as particles covered with the H_2O ice mantles. Thus, the line of $T = 160$ K represents the location of the H_2O snowline. This difference in the composition of the dust particles affects the dust growth. The results of the detailed dust evolution are presented in Section 3.1.2.

The upper left of Fig. 6 shows that the gas surface density in the range of $\gtrsim 3$ au increases with time during the infall phase. The gas surface density becomes very high due to the mass supply from the infalling envelope. Then, the gas disk is unstable against gravitational instability. The lower left panel of Fig. 6 indicates that Toomre Q parameter becomes $Q \lesssim 1.5$ for the outer disk region ($\gtrsim 3$ au). When gravitational instability develops in the disk, the angular momentum is transported by the gravitational torque. The lower right panel of Fig. 6 shows that the viscous alpha parameter $\alpha_{\rm SS}$ becomes high for the outer disk region where a gravitationally unstable state $Q \lesssim 1.5$ is realized. Thus, the gas disk expands due to gravitational torque. In the outer disk region, $Q \sim 1.5$ is maintained during the infall phase because the continuous mass supply from the infalling envelope increases the disk surface density. The angular momentum transport due to the disk gravitational instability controls the upper limit of the surface density (Takahashi et al. 2013).

The upper right panel of Fig. 6 shows the disk midplane temperature in the range $\gtrsim 3$ au increase with time during the infall phase. When the gas surface density is high, viscous heating becomes the dominant heating source of the disk. Thus, the disk temperature increases as the gas surface density increases. During the infall phase, the snowline moves outward with time. The location of the snowline affects the growth of dust particles (Section 3.1.2).

The upper panels of Fig. 6 show that the surface density and temperature in the inner disk region ($r \lesssim 3$ au) vary with time. The fluctuation in surface density and temperature is attributed to the outbursts. The inner region of the disk ($r \lesssim 3$ au) is stable against gravitational instability ($Q \gg 1$). When the transition from the quiescent phase to the outburst active phase occurs, the temperature becomes hot enough to activate MRI. The viscous alpha parameter $\alpha_{\rm SS}$ increases due to MRI and the mass accretion is enhanced. This causes fluctuations in the surface density and temperature in the inner disk region.

Next, the results of the gas evolution after the infall phase are presented. Figure. 7 shows the radial profile of the surface density, temperature, Toomre Q parameter, and viscous alpha parameter $\alpha_{\rm SS}$ at four different epochs after the infall phase. The upper

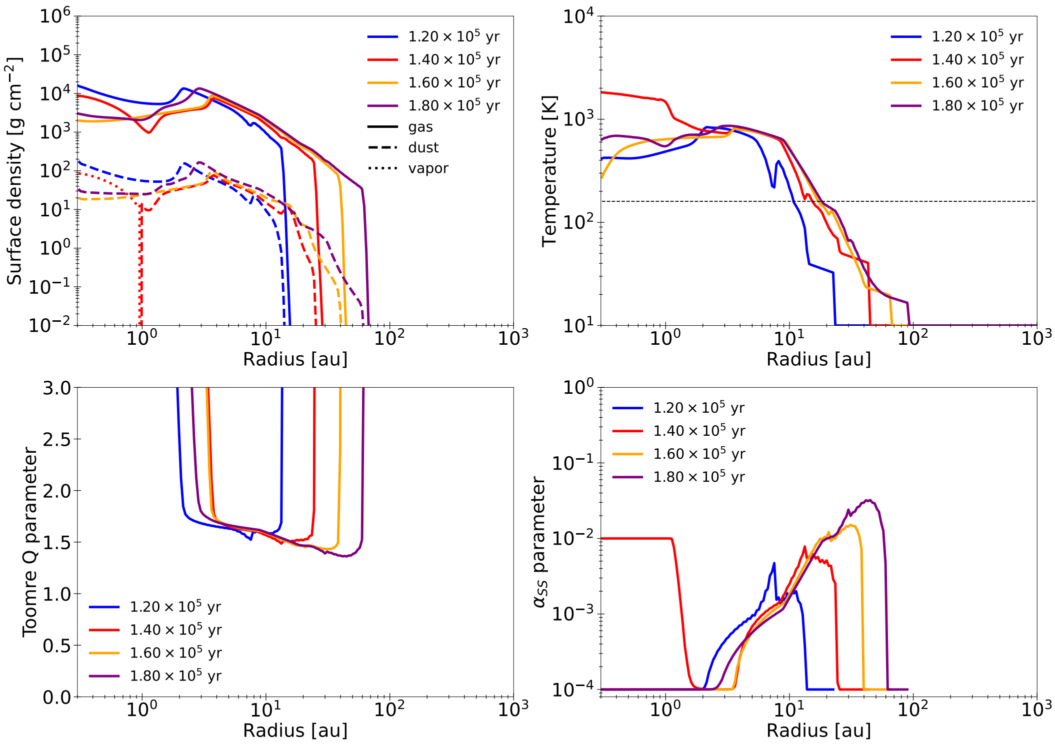

Figure 6. Time evolution during the infall phase of the radial profiles of surface density (upper left), temperature (upper right), Toomre Q parameter (lower left) and α parameter (lower right) for the case without disk wind.

left panel of Fig. 7 shows the gas surface density slightly decreases since there is no mass supply from the infalling envelope. As shown in the lower panels of Fig. 7, the outer disk region is still gravitationally unstable $Q \sim 1.5$–2 , and the gravitational torque primarily transports the angular momentum. As a result, the disk continues to expand after the infall phase. This implies that the disk mass remains relatively large for 10^5 years after the infall phase in the case without disk wind.

The upper right panel of Fig. 7 shows the temperature at different times after the infall phase. The viscous heating decreases as the gas surface density decreases. Thus, the temperature decreases and the snowline moves inward with time.

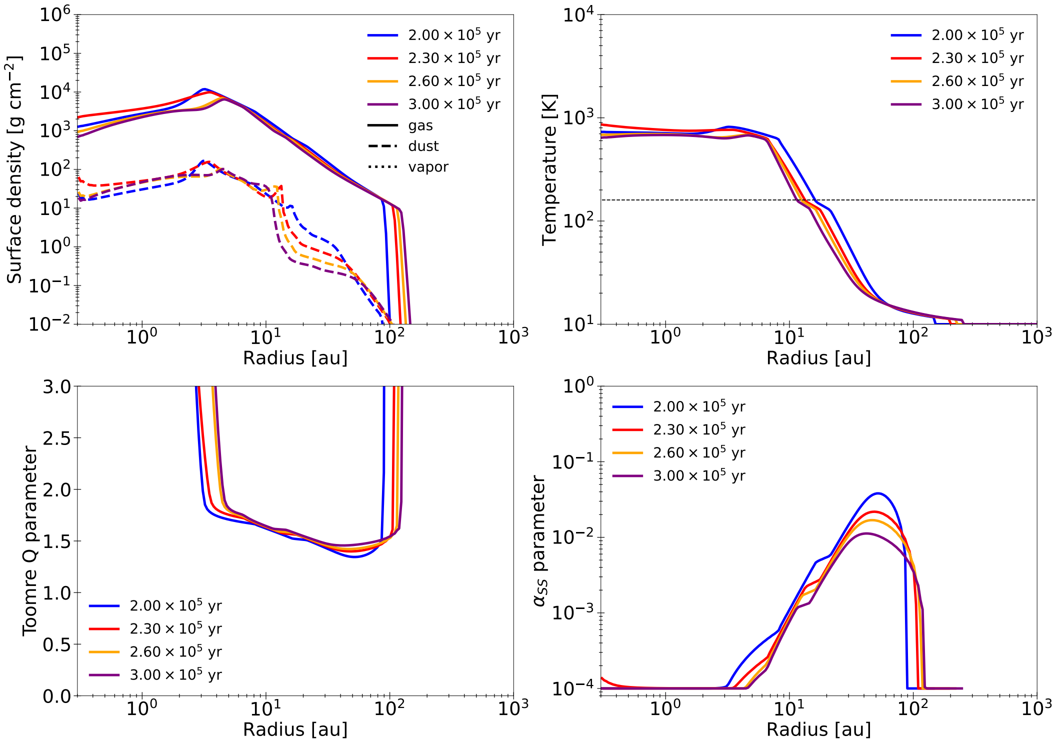

Figure 7. Time evolution after the infall phase of the radial profiles of surface density (upper left), temperature (upper right), Toomre Q parameter (lower left) and α parameter (lower right) for the case without disk wind.

3.1.2 Dust evolution without disk wind

This subsection describes the results of the dust evolution in the case without disk wind. The upper left panel of Fig. 6 shows the time evolution during the infall phase of the dust density (dashed lines) and the vapor surface density (dotted lines). In the inner disk region, the dust particles are coupled with gas particles since the gas density is relatively high. Therefore, the radial profile of the dust surface density in the inner disk region is almost the same as the gas surface density. When the temperature exceeds $T > 1500$ K, the dust particles evaporate, and the vapor increases. On the other hand, when the temperature is below 1500 K, the vapor condenses to the dust particles. Such evaporation and condensation occur repeatedly due to outbursts in the inner disk region.

The upper panel of Fig. 6 shows the dust surface density shows decreasing radial profiles in the range $\gtrsim 20$ au compared to the gas surface density. In the outer disk regions, the dust particles are (marginally) decoupled with the gas particles because of the dust growth by the collisional coagulation and the relatively low gas density. I confirm that the Stokes number of the grown dust particles with $a \sim 1$–10 cm is St ~ 0.01. Thus, the grown dust particles drift inward and the dust surface decreases.

Figure 8 shows the dust size distribution at four different epochs during the infall phase in the case without disk wind. In Fig. 8, the black solid line shows the dust particle size limited by the collisional fragmentation (the fragmentation barrier) (Birnstiel et al. 2012),

$$a_{\rm frag} = f_f \frac{2}{3\pi} \frac{\Sigma_{\rm g}}{\rho_{\rm di}\alpha_{\rm turb}} \frac{{v_{\rm frag}}^2}{c_s^2}, \tag{78}$$

where $f_f = 0.77$, and the black dashed line shows the dust particle size limited by the dust radial drift (the dust drift barrier) (Birnstiel et al. 2012),

$$a_{\rm drift} = f_d \frac{2\Sigma_{\rm d}}{\pi\rho_{\rm di}} \frac{r^2\Omega^2}{c_s^2} \left| \frac{{\rm d}\ln P}{{\rm d}\ln r} \right|^{-1}, \tag{79}$$

where $f_d = 0.55$. The location where $a_{\rm frag}$ increase in the step-function is corresponding to the snowline. Outside the snowline, H_2O ice particles can be presented. The fragmentation velocity of H_2O ice dust particles is larger than that of the silicate dust particles. Thus, $a_{\rm frag}$ outside the snowline is larger than that inside the snowline. The dust particle can grow up to $a_{\rm frag}$ as long as they do not suffer radial drift.

Figure 8 shows that the maximum size of dust particles is determined by collisional fragmentation inside the snowline and is about $a \sim 1$–10 cm. Inside the snowline, the dust particles cannot grow large enough because the fragmentation velocity of the silicate dust particle is low. On the other hand, outside the snowline, the maximum size of the dust particles is limited by the radial drift. The line of $a_{\rm frag}$ in Fig. 8 indicates that the dust particles can grow up to the maximum size $\sim 10^2$ cm outside the snowline. However, the dust particles move inward due to radial drift before they grow to the maximum size determined by collisional fragmentation $a_{\rm drift}$. Thus, the dust density outside the snowline decreases with time due to the radial drift of the grown dust particles (see also Fig. 6).

Figure 9 shows the dust-to-gas mass ratios at different times during the infall phase. In the upper panel of Fig. 9, the dust-to-gas mass ratios are calculated using the surface densities of gas and dust. In this study, the dust-to-gas mass ratio of the cloud core is set to be 0.01. During the infall phase, the dust-to-gas mass ratio calculated using the surface density does not change significantly in the range $\lesssim 20$ au and maintains ~ 0.01. On the other hand, in the outer disk region $\gtrsim 20$ au, the mass ratios decrease Compared to the initial mass rate 0.01 due to the radial drift of the grown dust particles, as described above. In the vicinity of the snowline, the mass ratios fluctuate slightly due to the accumulation of dust particles across the snowline.

In the lower panel of Fig. 9, the dust-to-gas mass ratios are calculated using the mass densities at the disk midplane of gas and dust. Compared to the mass ratio calculated using the surface density, the mass ratio at the disk midplane increases from the initial value of the core 0.01, especially inside the snowline. This is due to the settling of the growth dust particles onto the disk midplane.

Next, I describe the result of dust evolution after the infall phase in the case without disk wind. The upper left panel of Fig. 7 shows the time evolution after the infall phase of the dust density (dashed lines) and the vapor surface density (dotted lines). In the disk region inside the radius of 10 au, the radial profile of the dust surface density does not change significantly for 10^5 years after the infall phase. On the other hand, in the disk region outside of 10 au, the dust surface density decreases with time due to the radial drift of the grown dust particles.

Figure 8 shows the time evolution after the infall phase of the dust size distribution in the case without disk wind. As in the infall phase, the maximum size of dust particles inside the snowline is limited by fragmentation, while outside the snowline, the maximum size of the dust particles is determined by the radial drift. After the infall phase, since the supply of small dust particles to the disk from the infalling envelope, outside the snowline, the small dust particles in the disk are depleted with time due to the coagulation growth of dust particles. Dust particles that grow

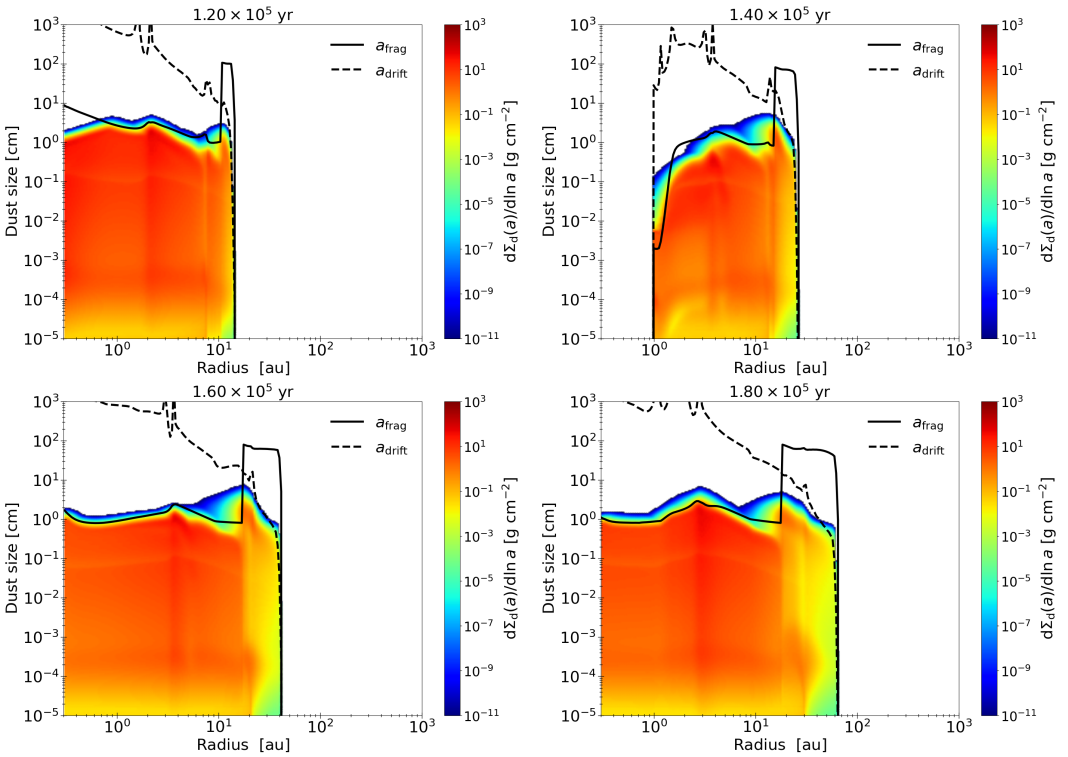

Figure 8. Time evolution during the infall phase of the dust size distribution in the case without disk wind. The black solid and dashed lines represent the dust particle size determined by the fragmentation and the radial drift, respectively.

outside the snowline drift inward and cross the snowline. Inside the snowline, the dust maximum size is limited by fragmentation and dust radial drift becomes weak.

Figure 11 shows the dust gas mass ratio calculated using the surface density (upper panel) and the mass density at the disk midplane (lower panel) after the infall phase. After the infall phase, dust to gas mass ratio outside the snow line decreases with time due to the strong radial drift of the dust particles as described above. In the vicinity of the snowline, the mass ratio is piled up as a result of an accumulation of dust particles that radially drift from outside the snowline. The mass ratio inside the snowline increases with time. At the end of the calculation, in the disk region within a radius of 3 au, the dust gas mass ratio is doubled when calculated using the surface density and three times when calculated using the midplane mass density from the initial value (0.01).

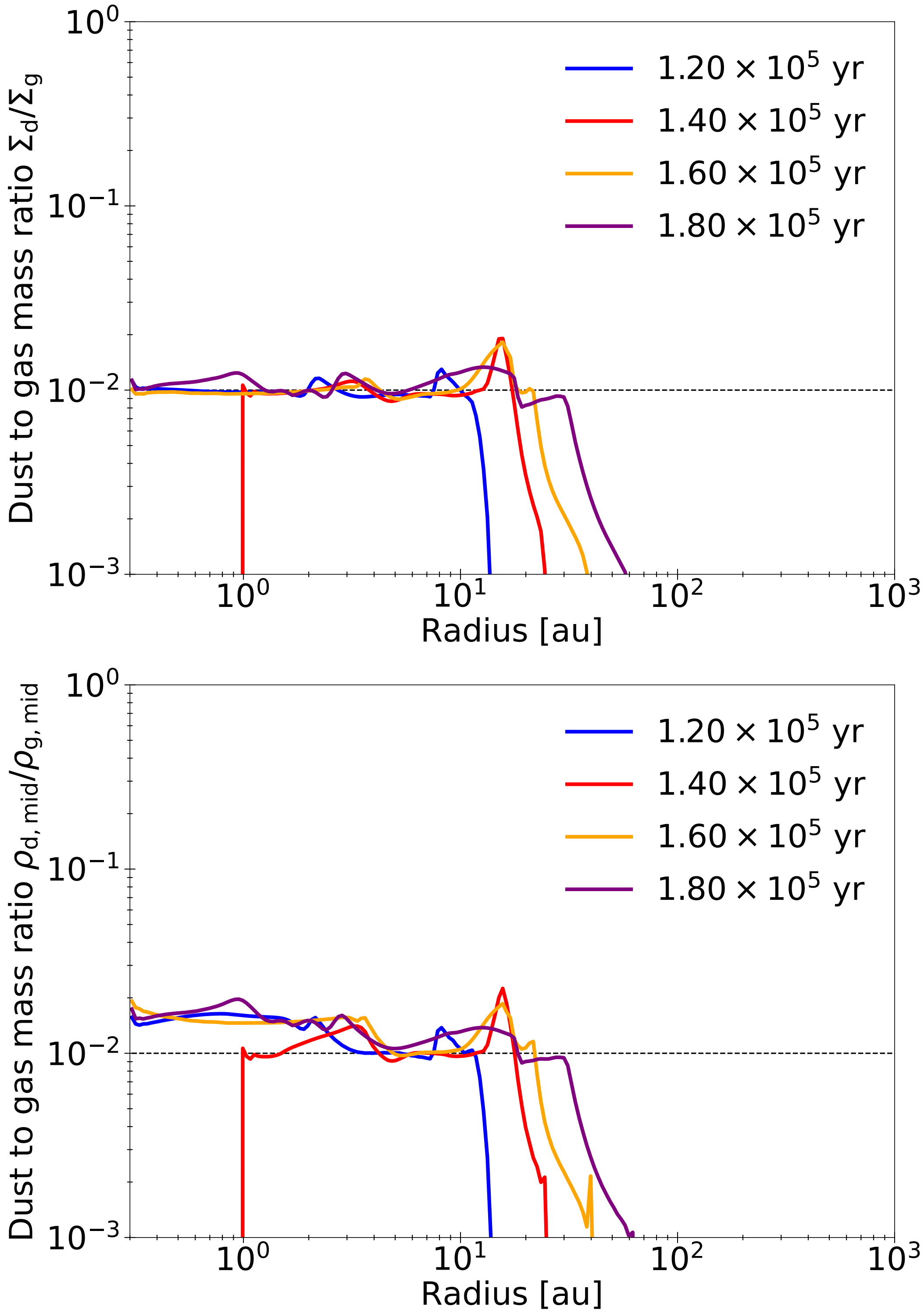

Figure 9. Time evolution during the infall phase of the dust-to-gas mass ratio in the case without disk wind. In the upper panel, the dust-to-gas mass ratios are calculated using the surface density of gas and dust. In the lower panel, the dust-to-gas mass ratio is calculated using the mass density at the disk midplane.

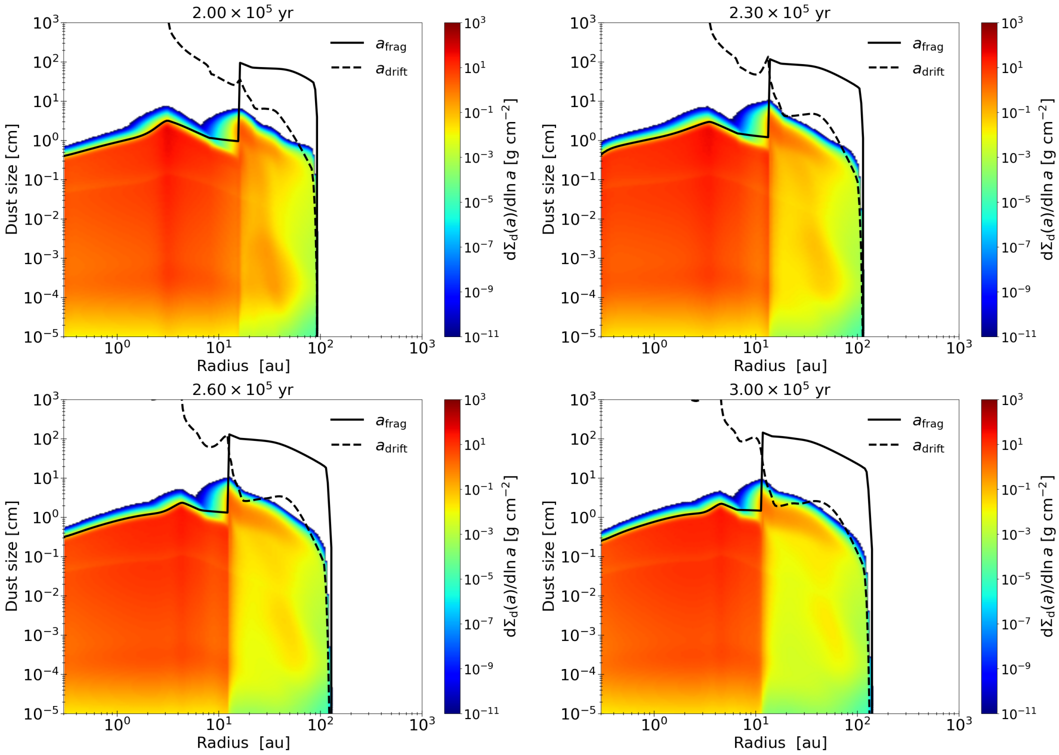

Figure 10. Time evolution after the infall phase of the dust size distribution in the case without disk wind.

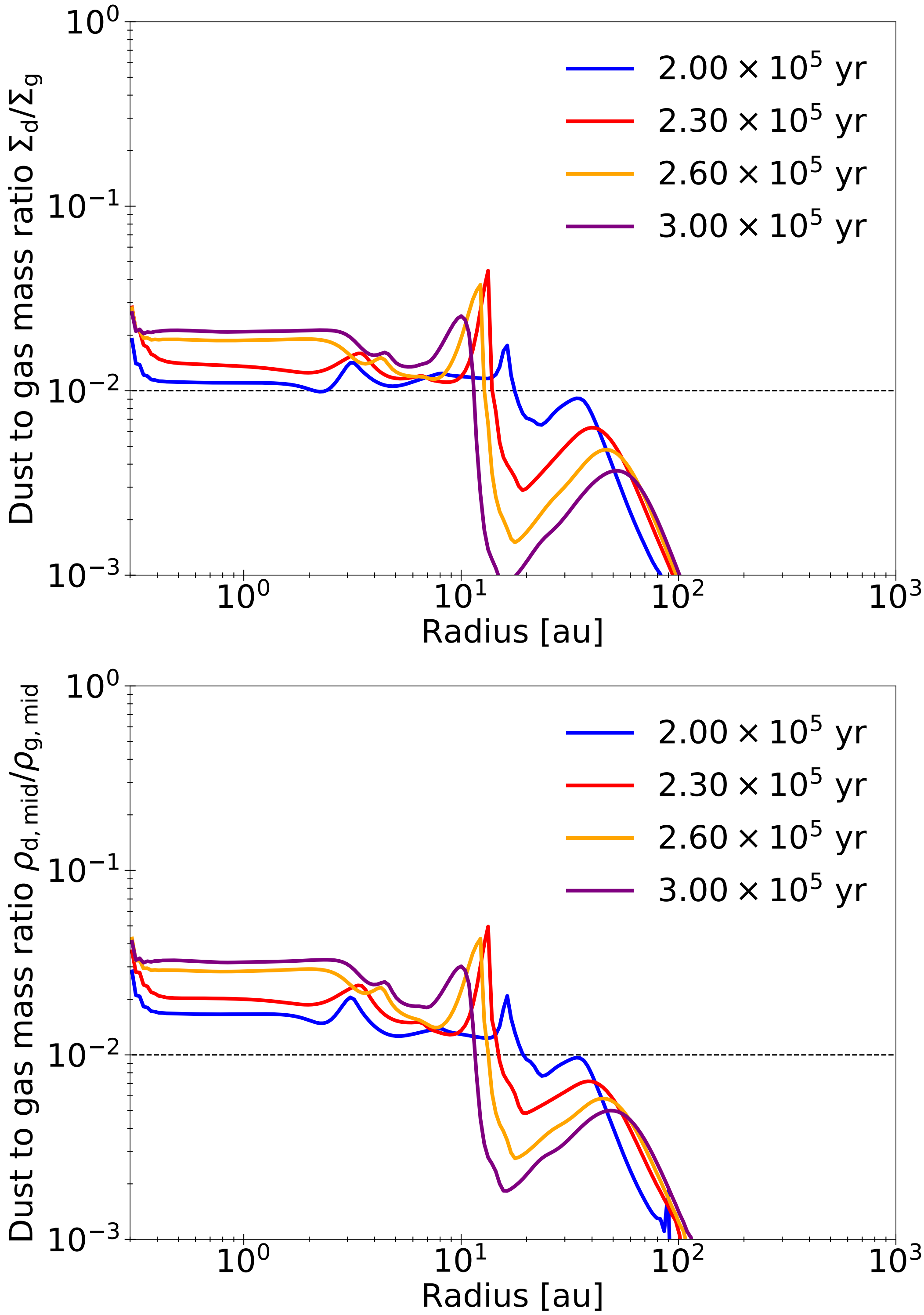

Figure 11. Time evolution after the infall phase of the dust-to-gas mass ratio in the case without disk wind

3.2 Case with disk wind

This subsection describes the results of the disk evolution with disk wind. The top panel of Fig. 12 shows the time evolution of the mass infall rate from the infalling envelope to the disk $\dot{M}_{\rm inf}$, the mass accretion rate from the disk to the star $\dot{M}_{\rm acc}$, and the mass loss rate from the disk by the disk wind $\dot{M}_{\rm wind}$. As described in Section 2.4, if the condition $\dot{\Sigma}_{\rm wind} > \dot{\Sigma}_{\rm inf}$ is satisfied, the disk wind is driven from the disk and the infalling gas is blown away by the wind. I have subtracted the infalling gas blown away by the wind from the total mass of gas infalling into the star–disk system. Thus, the infall rate $\dot{M}_{\rm inf}$ varies compared to the case without disk wind (Fig. 5).

The mass accretion rate from the disk to the central star $\dot{M}_{\rm acc}$ shows episodic behavior, as in the case without disk wind (Fig. 5). The magnitude of the peak of the outbursts is lower in the case with disk wind than in the case without disk wind. The outburst interval in the case with disk wind is as short as $\sim$ 700–800 years, which is shorter than in the case without disk wind. In contrast to the case without disk wind, no outbursts occur for $t \gtrsim 2.8 \times 10^5$ years with the disk wind.

During the infall phase, the wind mass loss rate maintains $4 \times 10^{-6}\ {\rm M}_\odot/{\rm yr}$ because the gas surface density is maintained by the mass supply from the infalling envelope. After the infall phase, since there is no mass infalling from the core and the surface density decreases, the wind mass loss rate decreases with time.

The middle panel of Fig. 12 shows the mass evolution of the disk, star, and wind. The total wind mass is larger than the disk mass at $t \sim 1.25 \times 10^5$ year, and then larger than the stellar mass at $t \sim 1.55 \times 10^5$. During the infall phase, the masses of the disk and the star are lower in the case with disk wind than in the case without disk wind. At the end of the infall phase, the star, the disk, and the wind mass are $M_{\rm star} \simeq 0.31\ {\rm M}_\odot$, $M_{\rm disk} \simeq 0.31\ {\rm M}_\odot$ and $M_{\rm wind} \simeq 0.39\ {\rm M}_\odot$, respectively, as described in Table 2. After the infall phase, the rates of increase of the masses of the star and wind are small as the disk mass decreases. At the end of the calculation, the masses of the star, disk, and wind are $M_{\rm star} \simeq 0.34\ {\rm M}_\odot$, $M_{\rm disk} \simeq 0.17\ {\rm M}_\odot$ and $M_{\rm wind} \simeq 0.49\ {\rm M}_\odot$, respectively. Thus, about 50% of the mass of the prestellar core is blown away from the central region by the disk wind, which means that the star formation efficiency is about 30% (for details, see Sec. 4.2).

The bottom panel of Fig 12 shows the time evolution of the stellar luminosity $L_\star$ and the accretion luminosity $L_{\rm acc}$ in the case with disk wind. During the infall phase, the accretion luminosity dominates the stellar luminosity. The accretion luminosity is lower in the case with disk wind than without disk wind. After the infall phase, the accretion luminosity decreases as the mass accretion rate decreases. After $t \sim 2.8 \times 10^5$ year, the accretion luminosity is lower than the stellar luminosity because outbursts, which enhance the accretion luminosity, do not occur.

3.2.1 Gas evolution with disk wind

This subsection describes the time evolution of the gas disk in the case with disk wind. Figure 13 shows the radial profile of the surface density, temperature, Toomre Q parameter, and viscous alpha parameter $\alpha_{\rm SS}$ in the case with disk wind at different epochs during the infall phase. Figure 14 the ratio of the wind mass loss rate to the mass infall rate $\dot{\Sigma}_{\rm wind}/\dot{\Sigma}_{\rm inf}$ against the disk radius. As described in 2.4, if $\dot{\Sigma}_{\rm wind}/\dot{\Sigma}_{\rm inf} > 1.0$ is realized, the disk wind is driven. In the region where the disk wind occurs, the disk wind transports both mass and angular momentum. Thus, the wind torque also promotes mass accretion in addition to the viscous torque.

The disk wind is present in the range ~ 0.3–10 au, and the wind driving region extends outward with time, as shown in Fig. 14. In addition, Fig. 14 shows that the mass loss rate is highly time-variant and has a local peak between 1 and 3 au. The upper panels of Fig. 13 show that within $\sim$ 2–3 au, the surface density and temperature vary significantly due to episodic accretion or outbursts. The wind driving condition depends on the disk surface density, as described in Section 2.4. Thus, the wind is absent when the surface density is low just after an outburst. On the other hand, the wind is present when the surface density is high in the quiescent phase (Vorobyov & Basu 2006), during which the surface density continues to increase before or after an outburst.

The decrease of the gas surface density due to the disk wind affects the disk midplane temperature. The upper right panel of Fig. 13 shows the disk midplane temperature during the infall phase. In the range of $\sim$ 1–10 au, the surface density is low due to mass loss by the disk wind and mass accretion by the wind torque (upper left panel of Fig. 13). The decrease in surface density suppresses viscous heating, which lowers the disk temperature (upper right panel of Fig. 13) and reduces the region where MRI is active (lower right panel of Fig. 13). Thus, the disk evolution in the region $\sim$ 1–10 au is controlled by the wind torque.

In the outer disk region ($r \gtrsim 10$ au), the disk wind is absent (Fig. 14). Thus, the lower two panels of Fig. 13 show that in such a region, the angular momentum is

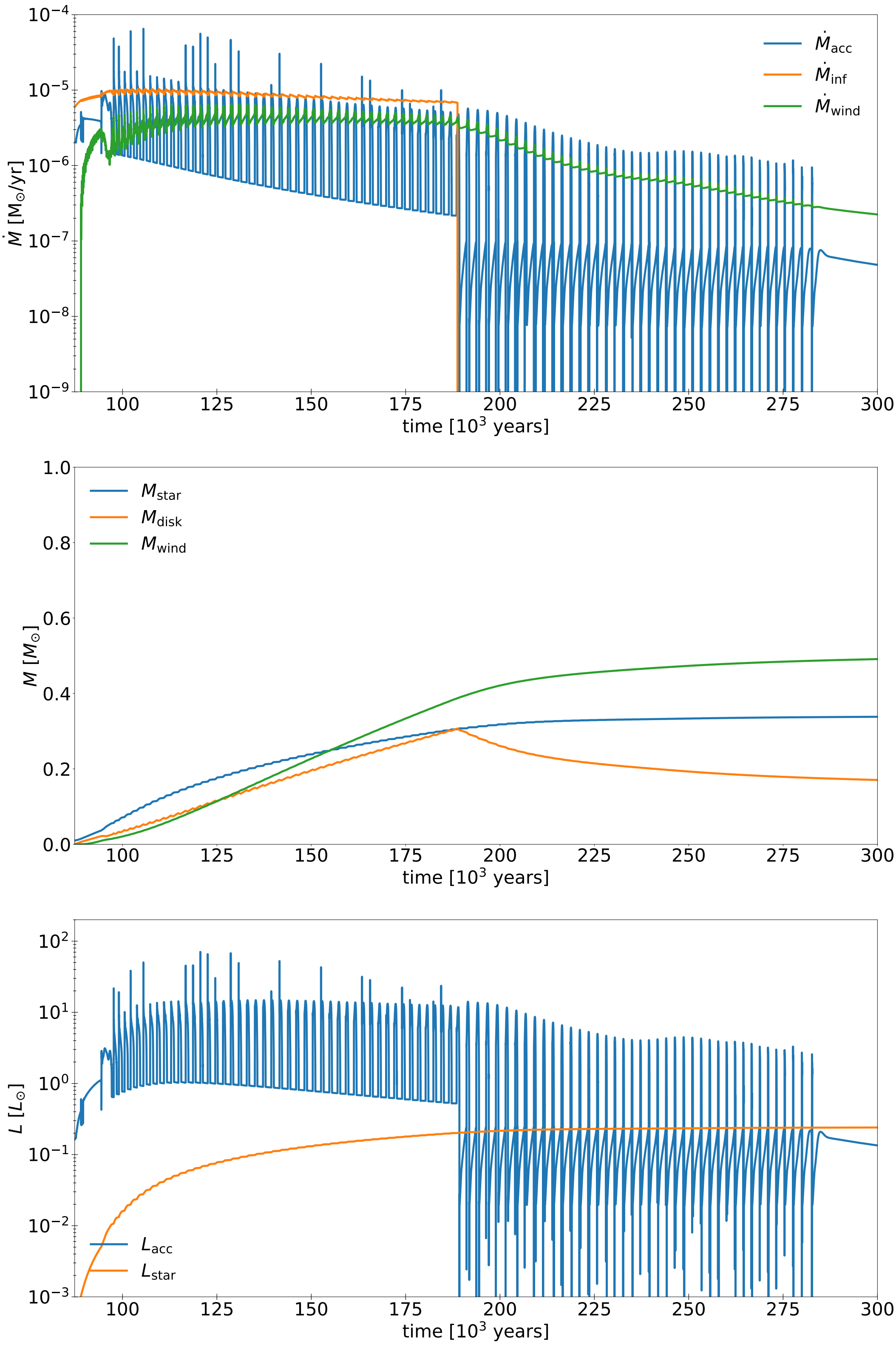

Figure 12. Time evolution of physical quantities in the case with disk wind. (Top) Mass accretion rate from the disk to the star $\dot{M}_{\rm acc}$, mass infall rate from the infalling envelope to the disk $\dot{M}_{\rm inf}$, and mass loss rate from the disk by the disk wind $\dot{M}_{\rm wind}$. (Middle) Masses of the disk $M_{\rm disk}$, central star $M_{\rm star}$, and disk wind $M_{\rm wind}$. (Bottom) Stellar internal luminosity $L_\star$ and accretion luminosity $L_{\rm acc}$.

redistributed primarily by the torque caused by the gravitational instability. Therefore, the disk evolves while maintaining a Toomre Q parameter of $Q \sim 1$–1.5 in the outer region as in the case without disk wind.

Next, I present the results of the gas evolution within the disk after the infall phase in the case with disk wind. Figure 15 shows the radial profiles of the surface density, temperature, Toomre Q parameter, and viscosity parameter α at different epochs after the infall phase in the case with disk wind. After the infall phase, the disk wind is present throughout the disk because the infalling gas, which suppresses the disk wind, has already dissipated. Thus, the upper left panel of Fig. 15 shows that the gas surface density decreases with time due to the disk wind. As seen from the lower panels of Fig. 15, the inner region of the disk ($r \lesssim 10$ au) is stable against gravitational instability. The disk wind becomes dominant in the inner disk region compared to the viscous diffusion. The effect of the disk wind tends to be more efficient on the inner region of the disk where the gas density and the temperature are larger, as described in equation (49). Thus, the upper left panel of Fig. 15 shows that the gas surface density of the inner disk is reduced by the disk wind compared to the outer disk region.

The upper right panel of Fig. 15 shows that the disk midplane temperature after the infall phase is lower in the case with disk wind than in the case without disk wind. This is because the viscous heating is suppressed by the decrease of the gas surface density due to the disk wind. We confirm that the viscous heating is dominant only in the disk region inside 10 au, while the irradiation heating is dominant outside 10 au at the end of the calculation $t = 3 \times 10^5$ year. The location of the snowline where $T = 160$ K migrates inward with time. In contrast to the case without disk wind, the snowline moves to the inside of the 10 au. This difference in the location of the snowline due to the presence of the disk wind affects the growth of dust particles after the infall phase (see Section 3.2.2).

The lower left panel of Fig. 15 shows that the Toomre Q parameter is $Q \lesssim 1.5$ in the outer region of the disk. The lower right panel of Fig. 15 shows that the viscous alpha parameter α_{SS} in the outer region of the disk is enhanced by the gravitational instability. Thus, the disk continues to expand after the infall phase even in the case with disk wind.

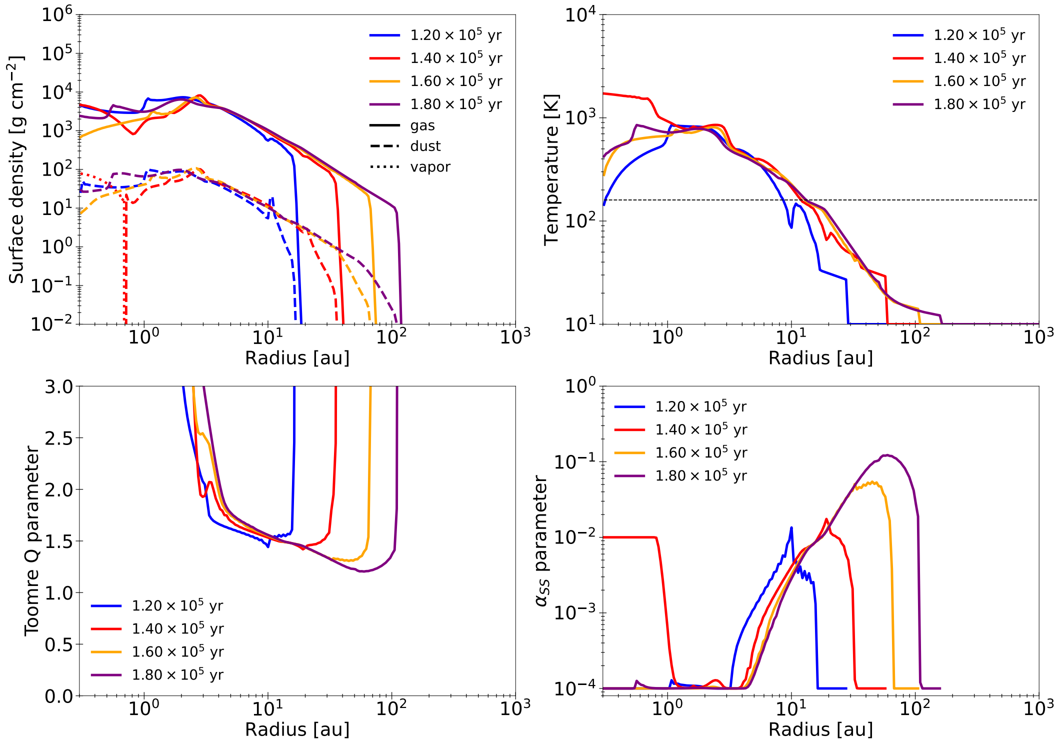

Figure 13. Time evolution during the infall phase of the radial profiles of surface density (upper left), temperature (upper right), Toomre Q parameter (lower left) and α parameter (lower right) for the case with disk wind.

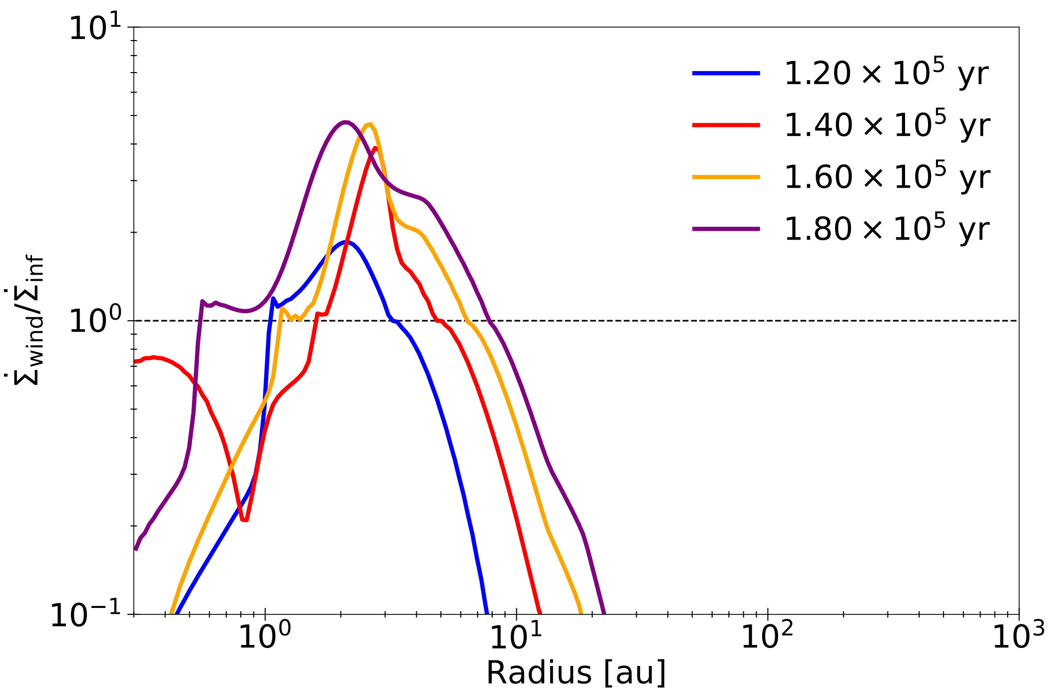

Figure 14. Ratio of the wind mass loss rate $\dot{\Sigma}_{\rm wind}$ to the mass infall rate $\dot{\Sigma}_{\rm inf}$ against the radius.

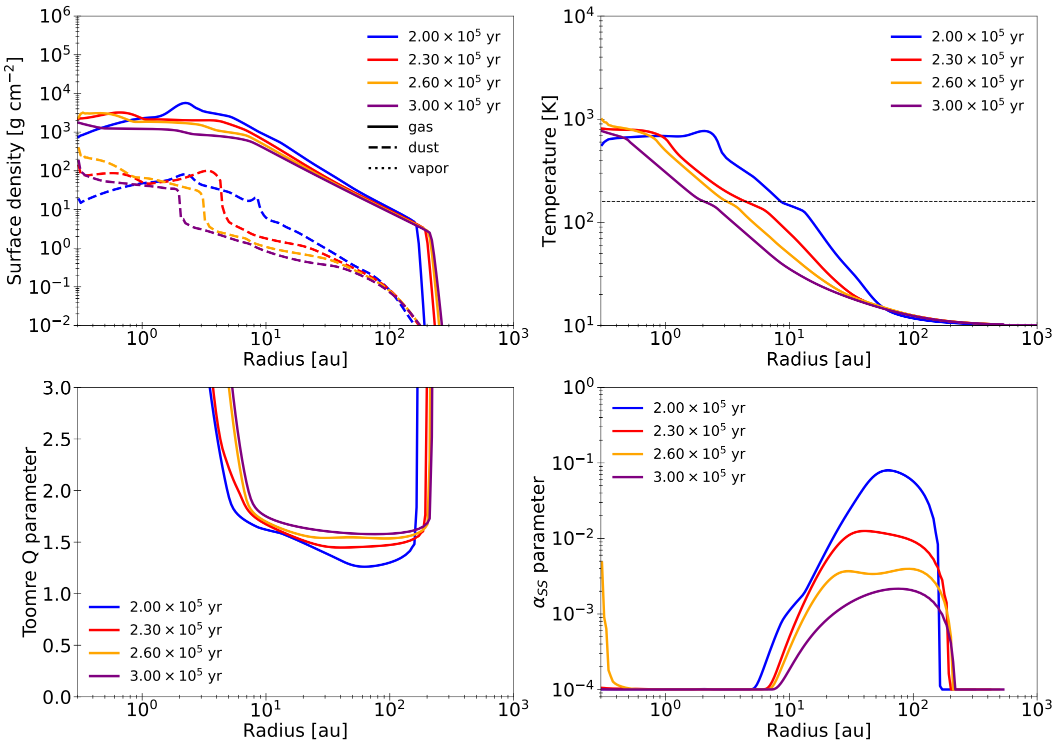

Figure 15. Time evolution after the infall phase of the radial profiles of surface density (upper left), temperature (upper right), Toomre Q parameter (lower left) and α parameter (lower right) for the case with the disk wind.

3.2.2 Dust evolution with disk wind

This subsection describes the results of the dust evolution in the case with disk wind. The upper left panel of Fig. 13 plots the dust (dashed lines) and vapor (dotted lines) surface density at four different times during the infall phase. The radial profile of the dust surface density is similar to that of the gas surface density. When the outbursts occur and the disk temperature exceeds 1500 K, the dust particles evaporate, and the vapor increases.

Figure 16 shows the times evolution during the infall phase of the dust size distribution in the case with disk wind. As in the case without disk wind, the maximum dust size of dust particles is limited by the fragmentation inside the snowline and by the radial drift outside the snowline. There is no significant difference in the evolution of the dust size distribution between with and without the disk wind. This is because the gas density is maintained due to the supply of gas to the disk even if the disk wind is present. Additionally, the fact that the snowline is located beyond 10 au during the infall phase is also a factor in the lack of significant differences in the dust size distribution between without and with disk wind.

Figure 17 shows the dust-to-gas mass ratio calculated using the surface density

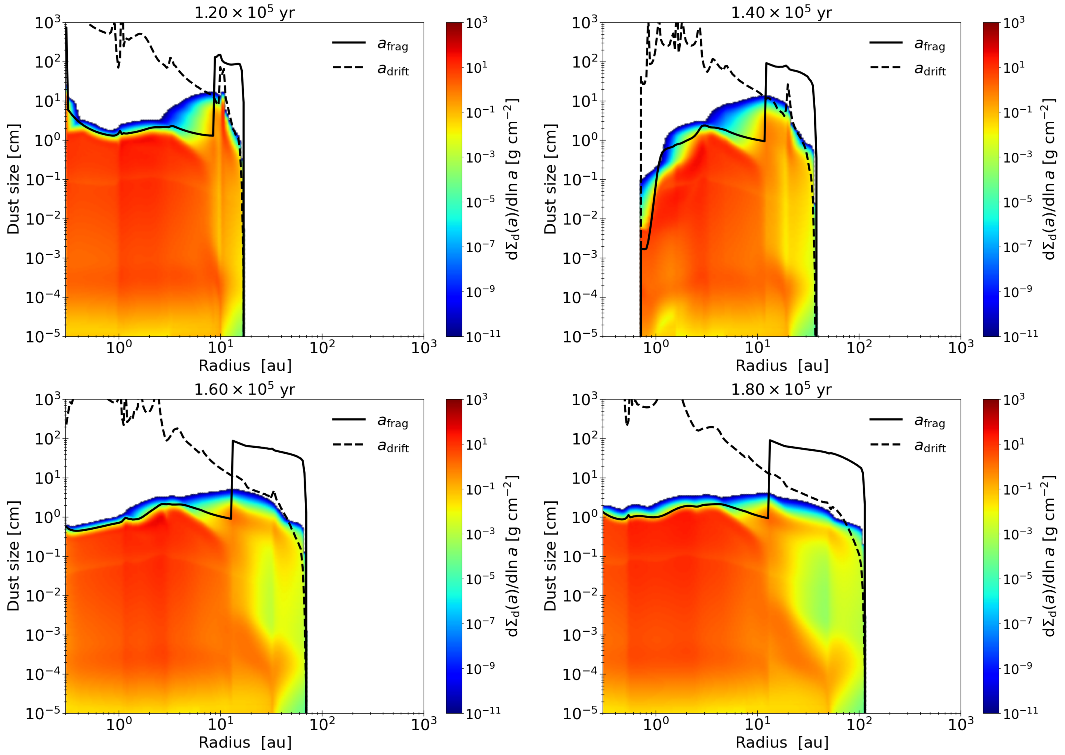

Figure 16. Time evolution during the infall phase of the dust size distribution in the case with disk wind.

(upper panel) and the mass density at disk midplane (lower panel) in the case with the disk wind. As described in Section 3.2.1, the disk wind is driven in the inner disk region of $\lesssim$ 10 au. In this study, only the small dust particles that satisfy St $< 10^{-4}$ are assumed to be removed with the gas from the disk by the disk wind. However, the contribution of these small dust particles to the total dust mass density in the disk is small. On the other hand, the mass loss of gas due to the disk wind is larger than that of dust particles. As a result, in the disk region where the disk wind is driven, the mass ratio becomes larger in the case with disk wind than in the case without disk wind. At $t = 1.2 \times 10^5$ year, the sharp enhancement of the mass ratio is seen at $\sim$ 10 au. This is probably due to the effect of the temperature maxima at 10 $\sim$ (upper right panel of Fig. 13). In the subsequent evolution, the enhancement disappears.

Next, I describe the results of the dust evolution after the infall phase in the case with disk wind. The upper left panel of Fig. 15 plots the dust surface density at four different epochs after the infall phase. As described above, the location of the snowline migrates inward with time after the infall phase. Outside the snowline, the dust particles can grow to a larger size and radially drift inward. In the case with disk wind, the snowline exists at a smaller radius compared to the case without disk

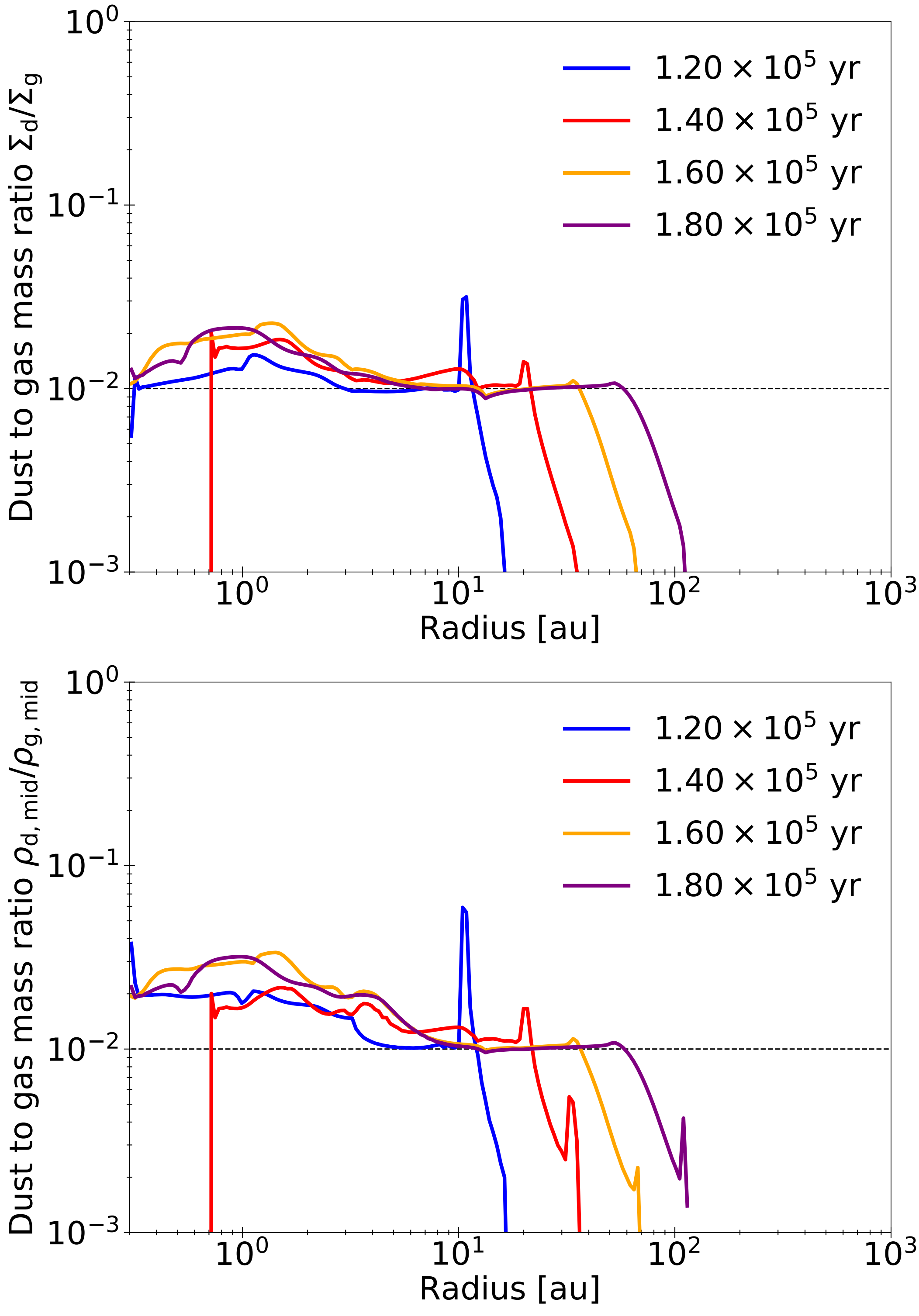

Figure 17. Time evolution during the infall phase of the dust-to-gas mass ratio in the case with disk wind

wind. Consequently, the dust surface density outside the snowline decreases with time.

Figure 18 shows the time evolution of the dust size distribution after the infall phase in the case with disk wind. Outside the snowline, dust particles can grow due to the high collisional fragmentation velocity. Due to the higher density in the inner regions of the disk, the collision frequency of dust particles increases, facilitating the growth of dust particles. As a result, as the snowline migrates toward the center, the maximum size of dust particles becomes larger. At the end of the calculation ($t = 3 \times 10^5$ year), the maximum size of dust particles is approximately ~ 50 cm at the snowline ($\sim$ 2au). While dust can grow significantly outside the snowline, the maximum size of dust particles is still constrained by radial drift. Outside the snowline, small dust particles are depleted due to coagulation growth.

The maximum size of dust particles inside the snowline is restricted by collisional fragmentation, typically around ~ 1 cm. Small dust particles are well coupled with the gas, preventing significant inward drift toward the center. As a result, the dust surface density inside the snowline is higher compared to outside the snowline.

The upper panel of Figure 19 shows the time evolution of the dust-to-gas mass ratio, calculated using the surface densities of gas and dust. The surface density ratio falls below 0.01 outside the snowline. On the other hand, inside the snowline, the mass ratio is significantly higher compared to the case without disk wind. In the inner edge region (~ 0.3 au), the mass ratio reaches around ~ 0.1.

The lower panel of Figure 19 shows the time evolution of the dust-gas-mass ratio, calculated using the mass density at the disk midplane. In contrast to the upper panel, the mass ratio, excluding the outermost edge of the disk, exceeds 0.01. The increase in mass ratio is attributed to both the mass loss due to the disk wind and the sedimentation of growth dust particles to the disk midplane. There is a tendency for the mass ratio to be higher toward the inner regions of the disk, with disk regions exceeding a mass ratio of 0.1. These results suggest that the disk wind is expected to sufficiently enhance the dust-to-gas mass ratio after the infall phase.

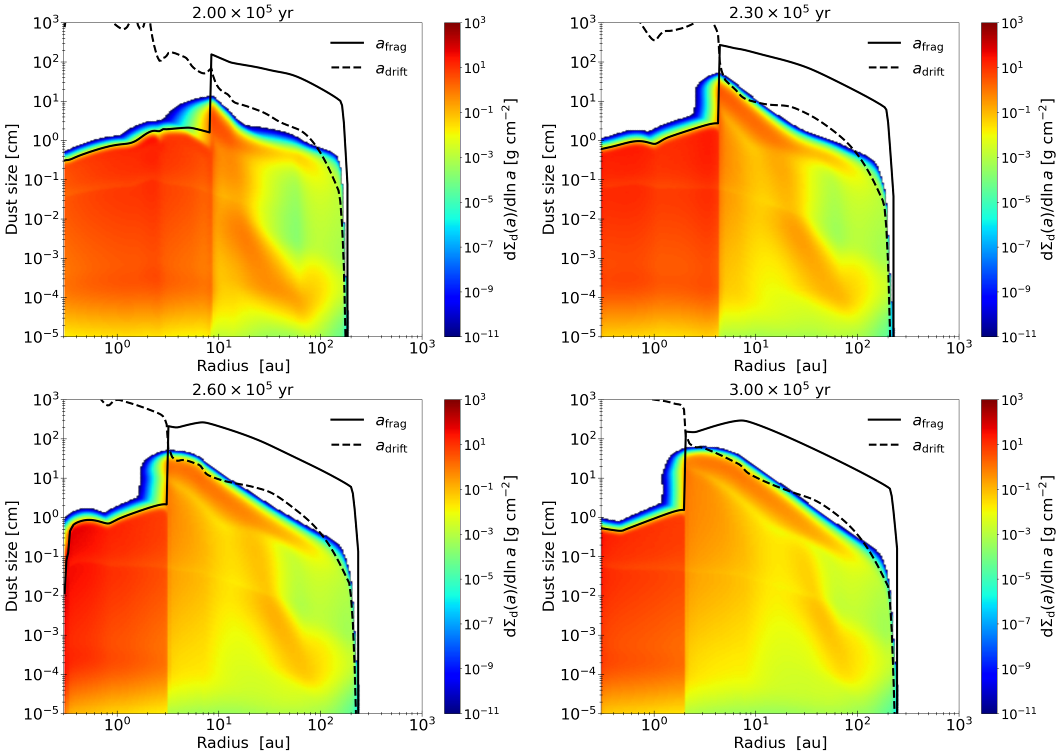

Figure 18. Time evolution after the infall phase of the dust size distribution in the case without disk wind.

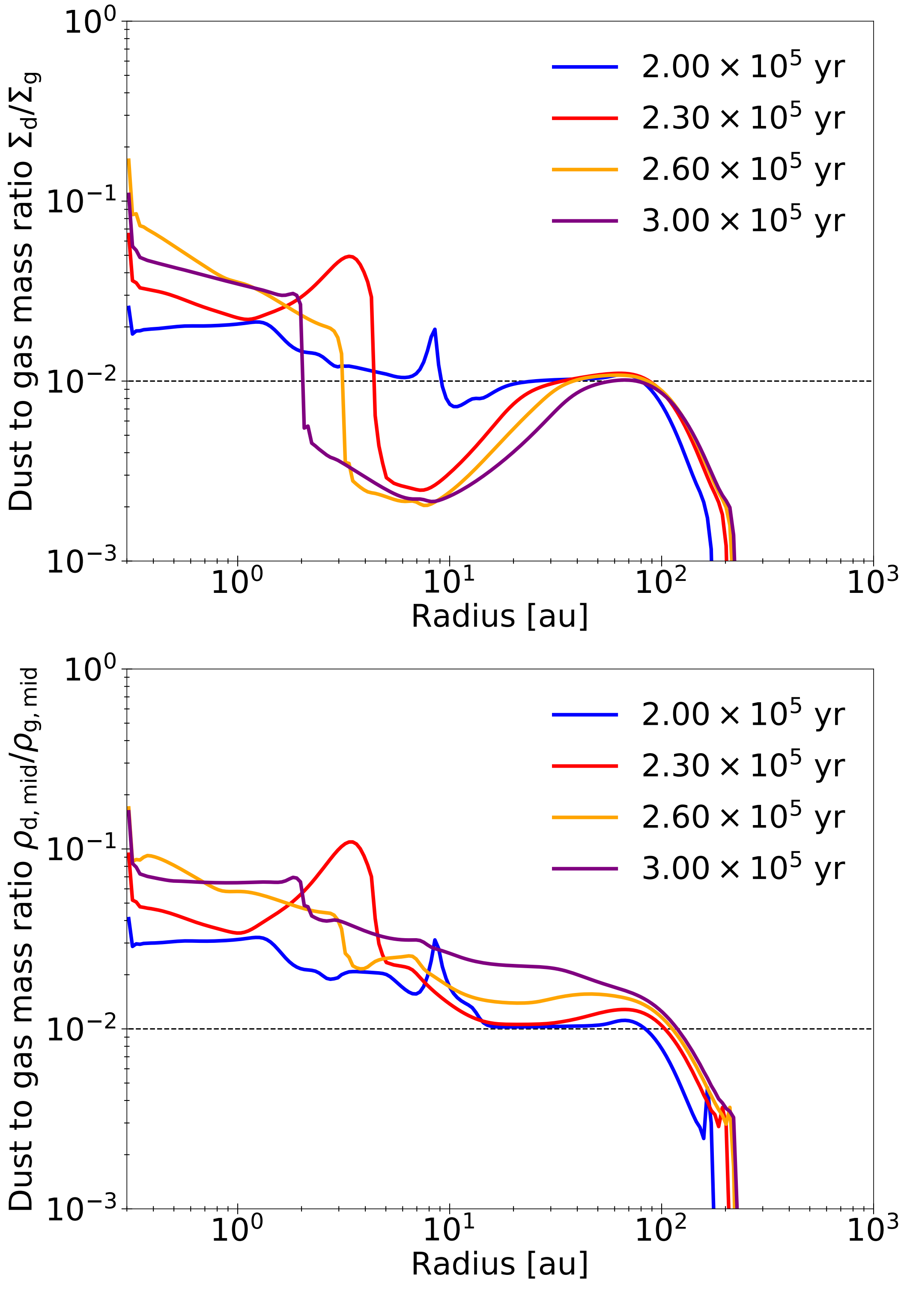

Figure 19. Time evolution after the infall phase of the dust-to-gas mass ratio in the case with disk wind

3.3 Comparison of calculations between cases with and without disk wind

In this subsection, I compare calculation results in the cases with and without a disk wind. Initially, I describe the comparison of the mass evolution of the disk and the central star, followed by the properties of the disk, and finally, the size of the dust particles.

3.3.1 Comparison of mass evolution between cases with and without disk wind

The upper panel of Figure 20 shows the mass evolution of the star, disk, and disk wind, comparing cases with and without disk wind. The vertical dotted lines in Fig. 20 indicate the end of the infall phase ($t \simeq 1.89 \times 10^5$ year). In the case without disk wind, fluctuations in the mass evolution of the star and disk primarily occur during outbursts. During the infall phase, the disk mass increases due to the mass supply from the infalling envelope. At the end of the infall phase, the stellar mass is larger than the disk mass in the case without disk wind. After the infall phase, the disk mass decreases due to the mass accretion onto the center star, especially when outbursts occur.

In the case with disk wind, during the early stages of the infall phase ($t \lesssim 10^5$ years), the influence of the disk wind on the mass evolution of the star and the disk is minimal. As the disk grows, the impact of the disk wind becomes apparent. During the infall phase, the rate of mass increase in the star gradually decreases compared to that of the disk. At the end of the infall phase, the masses of the star and the disk become comparable in the case with disk wind. The disk wind used in this study is an increasing function of the surface density and the disk temperature. Therefore, after the infall phase, the mass loss rate due to the disk wind decreases. Consequently, the reduction in the disk mass after the infall phase becomes gradual.

The lower panel of Figure 20 shows the time evolution of the masses of dust and vapor within the disk. The mass of dust within the disk is smaller in the case with disk wind than in the case without disk wind. This is because the dust infalling onto the disk is blown away along with gas by the disk wind, resulting in a reduced influx of dust into the disk.

The episodic decreases in dust mass evolution are due to the evaporation of dust particles caused by increases in disk temperature during outbursts. The decrease due to dust evaporation is accompanied by an increase in vapor. These episodic decreases in dust (or increases in vapor) are larger in the case with disk wind than in the case with disk wind. This is because the case without disk wind results in higher disk mass and temperature, and the region where the temperature exceeds 1500 K is broader compared to the case with disk wind.

After the infall phase, in the case with disk wind, the mass of dust within the disk decreases more compared to the case without disk wind. Figure 21 plots the time evolution of the mass accretion rate of dust onto the central star in the cases with and without disk wind, and the mass loss rate of dust due to disk wind. The mass accretion rate of dust is larger in the case with disk wind than that in the case without disk wind, especially after the infall phase ($t \gtrsim 1.89 \times 10^5$ years). The mass loss rate of dust due to the disk wind is also larger than the mass accretion rate in the case without disk wind. Thus, the rate of decrease of dust within the disk is larger in the case with disk wind than in the case without disk wind. In the case with disk wind, until 2.5×10^5 years after the infall phase, the loss of dust mass due to the disk wind is predominant. On the other hand, after 2.5×10^5 years, the accretion rate of dust onto the star becomes comparable to the mass loss rate due to the disk wind.

As described in 3.2.2, in the case with disk wind, the snowline moves closer to the center, making it easier for dust particles to grow. Due to the radial drift of the growth dust particles, a significant amount of dust is supplied to the inner region of the disk. As a result, after the infall phase, the mass accretion rate of dust onto the star increases with time. The disk wind torque also contributes to the higher mass accretion of dust compared to the case without disk wind.

After the infall phase, the mass loss rate due to the disk wind decreases with time. Therefore, beyond 2.8×10^5 years, the accretion rate of dust becomes more prominent than the mass loss rate due to the disk. However, it is worth noting that in this study, there is a restriction on the dust particles removed from the disk by the disk wind, specifically limited to $\mathrm{St} < 10^{-4}$.

Figure 22 shows the time evolution of the dust-to-gas mass ratio within the disk. In the case without disk wind, the mass ratio fluctuates due to the dust evaporation caused by the outbursts; however, it averages around ~ 0.095 during the infall phase. After the infall phase, the mass ratio continues to decrease.

In the case with disk wind, the mass ratio oscillates due to outbursts until

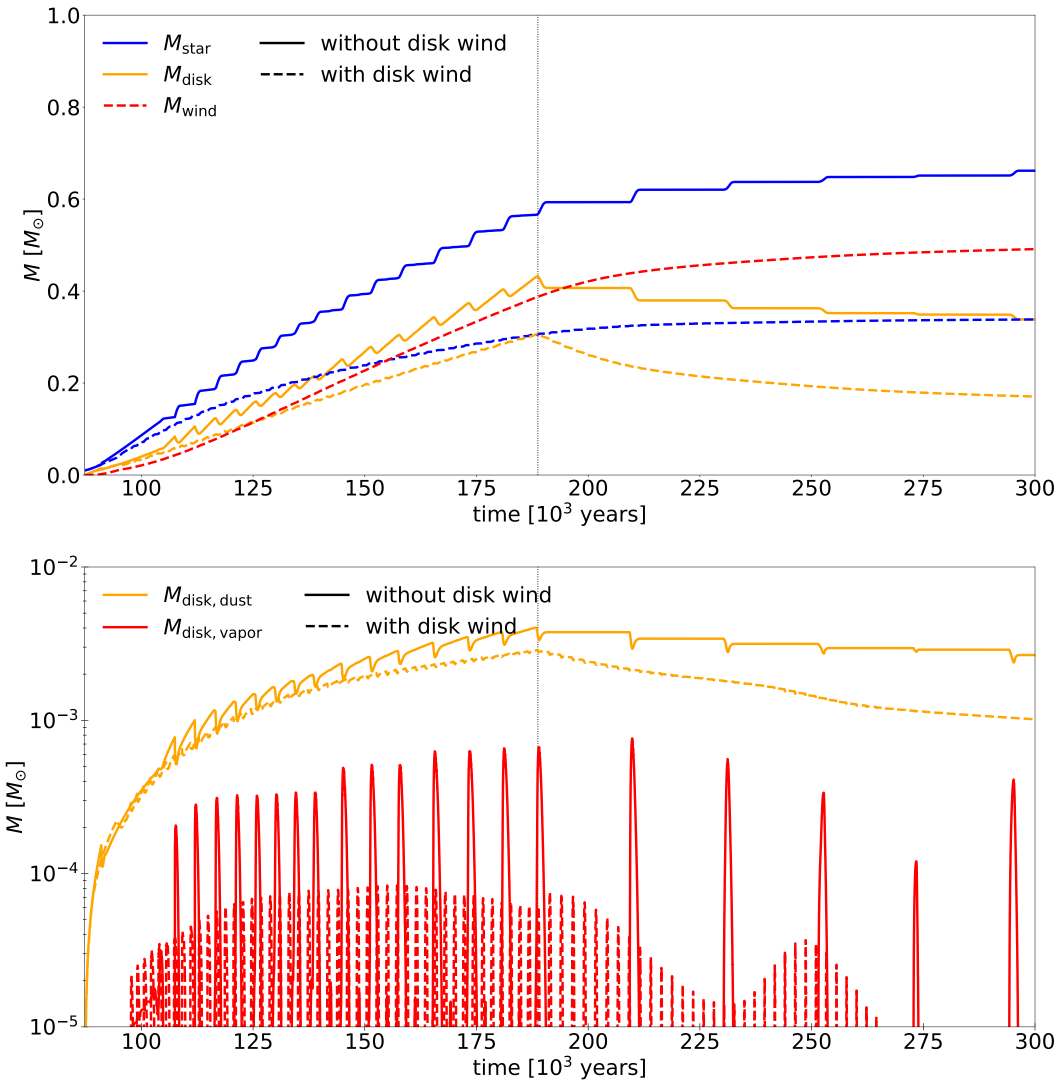

Figure 20. Time evolution of the masses of the disk, the central star, and the disk wind.

1.5×10^5 years, remaining at approximately 0.01. After $t \sim 1.5 \times 10^5$ year, the mass ratio slightly decreases to around ~ 0.095. After the infall phase, the mass ratio decreases more compared to the case without disk wind.

3.3.2 Comparison of disk evolution between cases with and without disk wind

In this section, I compare disk evolution in the cases with and without disk wind. Figure 23 plots the time evolution of the disk temperature, disk radius, Toomre Q parameter, and alpha parameter of GI $\alpha_{\rm GI}$. The vertical line in Fig. 23 corresponds to the epoch at which the infall phase ends. I defined the disk temperature, Toomre

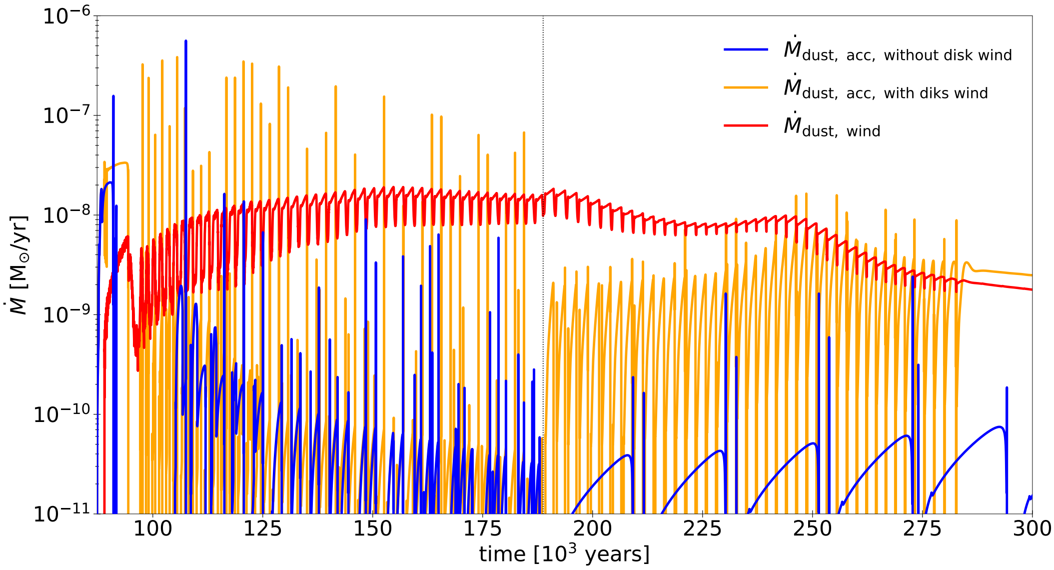

Figure 21. Time evolution of the mass accretion rate of dust and the loss mass of dust due to disk wind.

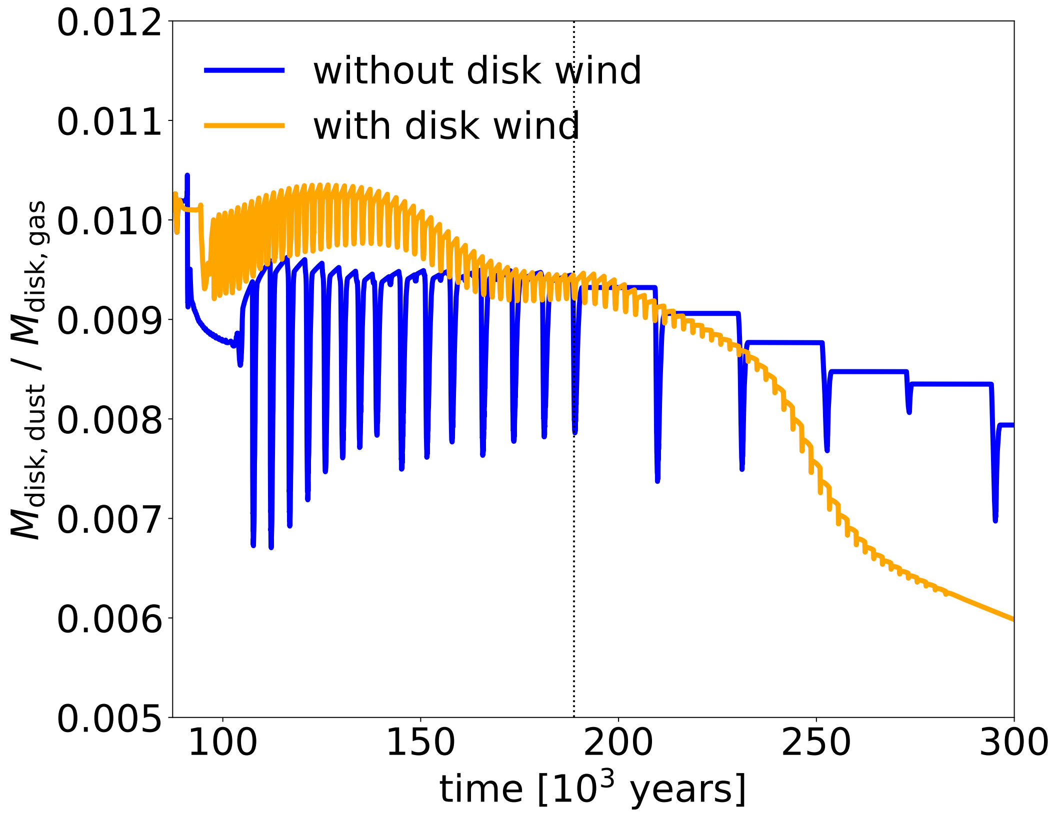

Figure 22. Time evolution of the total dust-to-gas mass ratio.

Q parameter, and alpha parameter of GI as mass-weighted averages,

$$\bar{F} = \frac{\int_{r>5\rm au} F\Sigma \mathrm{d}S}{\int_{r>5\rm au} \Sigma\, \mathrm{d}S} \tag{80}$$

where $F = T$, Q, and $\alpha_{\rm GI}$.

The upper left panel of Fig. 23 shows that the disk temperature with disk wind is lower than that without disk wind. The lower disk temperature affects the Toomre Q parameter or the gravitational stability of the disk. In the case with disk wind, the viscous heating rate decreases due to the mass loss. Thus, the disk temperature becomes low compared with the case without disk wind. On the other hand, the mass loss due to the disk wind tends to increase the Toomre Q parameter. However, during the infall phase, the disk mass does not change significantly, because of the continuous mass supply from the infalling envelope. As a result, the Toomre Q parameter maintains a lower value in the case with disk wind during the infall phase. In addition to the lower disk temperature, the lower mass of the central star also contributes to maintaining the lower value of the Toomre Q parameter.

Since the viscous alpha parameter of GI used in this study is sensitive to the Toomre Q parameter ($\alpha_{\rm GI} = \exp(-Q^4)$), the angular momentum transport is more efficient in the case with disk wind, as shown in the lower right panel of Fig. 23. Thus, during the infall phase, the disk radius is larger in the case with disk wind than in the case without disk wind (upper right panel of Fig. 23).

After the infall phase, in the case with disk wind, the disk mass decreases due to the mass loss by the disk wind. Thus, as shown in the lower right panel of Fig. 23, the Toomre Q parameter becomes larger in the case with disk wind than in the case without disk wind. As a result, the subsequent disk evolution with disk wind is expected to be controlled by the disk wind torque.

3.3.3 Comparison of dust size evolution between cases with and without disk wind

In this section, I compare the time evolution of dust particle sizes in the cases with and without disk wind. Figure 24 plots the time evolution of the average dust particle size at the disk radius of 5 au, 10 au, and 20 au. The average dust mass is calculated by

$$\langle m \rangle = \frac{\int m \frac{\mathrm{d}\Sigma_{\rm d}}{\mathrm{d}m} \mathrm{d}m}{\int \frac{\mathrm{d}\Sigma_{\rm d}}{\mathrm{d}m} \mathrm{d}m}, \tag{81}$$

and then computing the average dust size under the assumption of compact spheres,

$$\langle a \rangle = \left(\frac{3\langle m \rangle}{4\pi\rho_{\rm di}} \right)^{1/3}. \tag{82}$$

Fig. 24 shows that during the infall phase, the dust size is not significantly

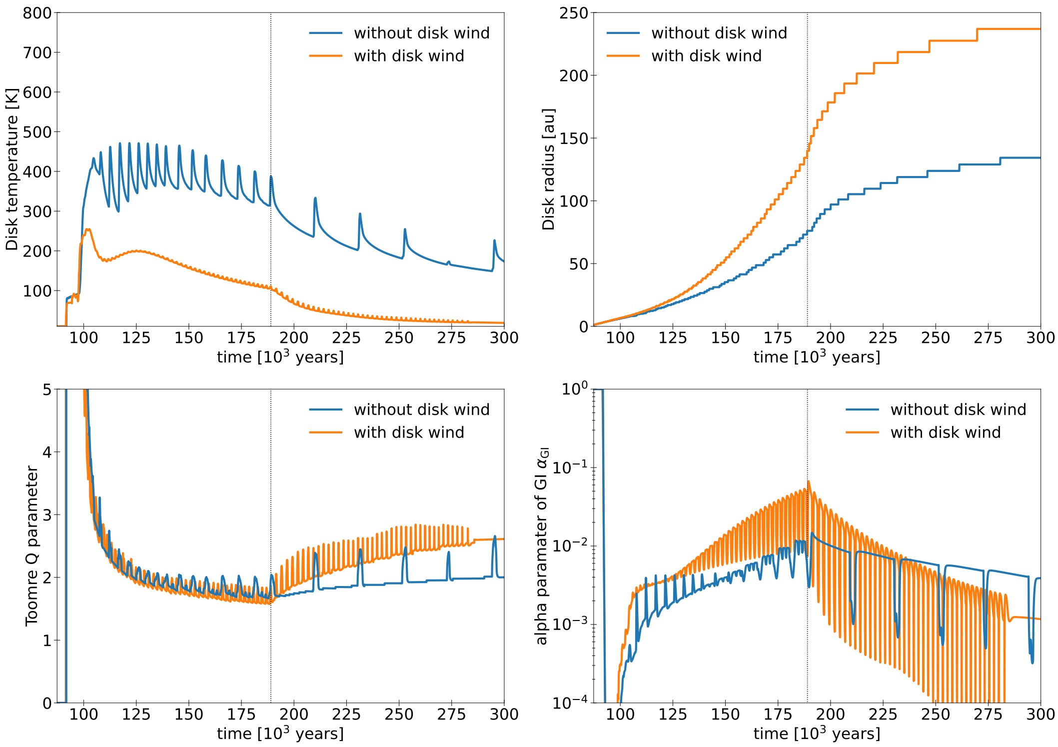

Figure 23. Time evolution of the disk temperature (upper left), disk radius (upper right), Toomre Q parameter (lower right), and alpha parameter of GI $\alpha_{\rm GI}$ (lower right) with and without disk wind. The vertical dotted line corresponds to the epoch at which the infall phase ends.

influenced by the presence or absence of a disk wind. After the infall phase, in the case without disk wind, the snowline remains beyond 10 AU until the end of the calculation at 3×10^5 years, as described in Section 3.1.2. As a result, dust growth is inhibited by collisional fragmentation inside the snowline. Therefore, within the disk radius of 10 au, the size of the dust particles remains nearly unchanged compared to the infall phase in the case without disk wind.

On the other hand, in the case with disk wind, the dust particles undergo significant collisional growth compared to the case without disk wind. This is because the disk temperature decreases, causing the snowline to move inward. Dust growth after the infall phase occurs from the outside to the inside of the disk because the snowline moves from the outside of $\gtrsim$ 10 au.

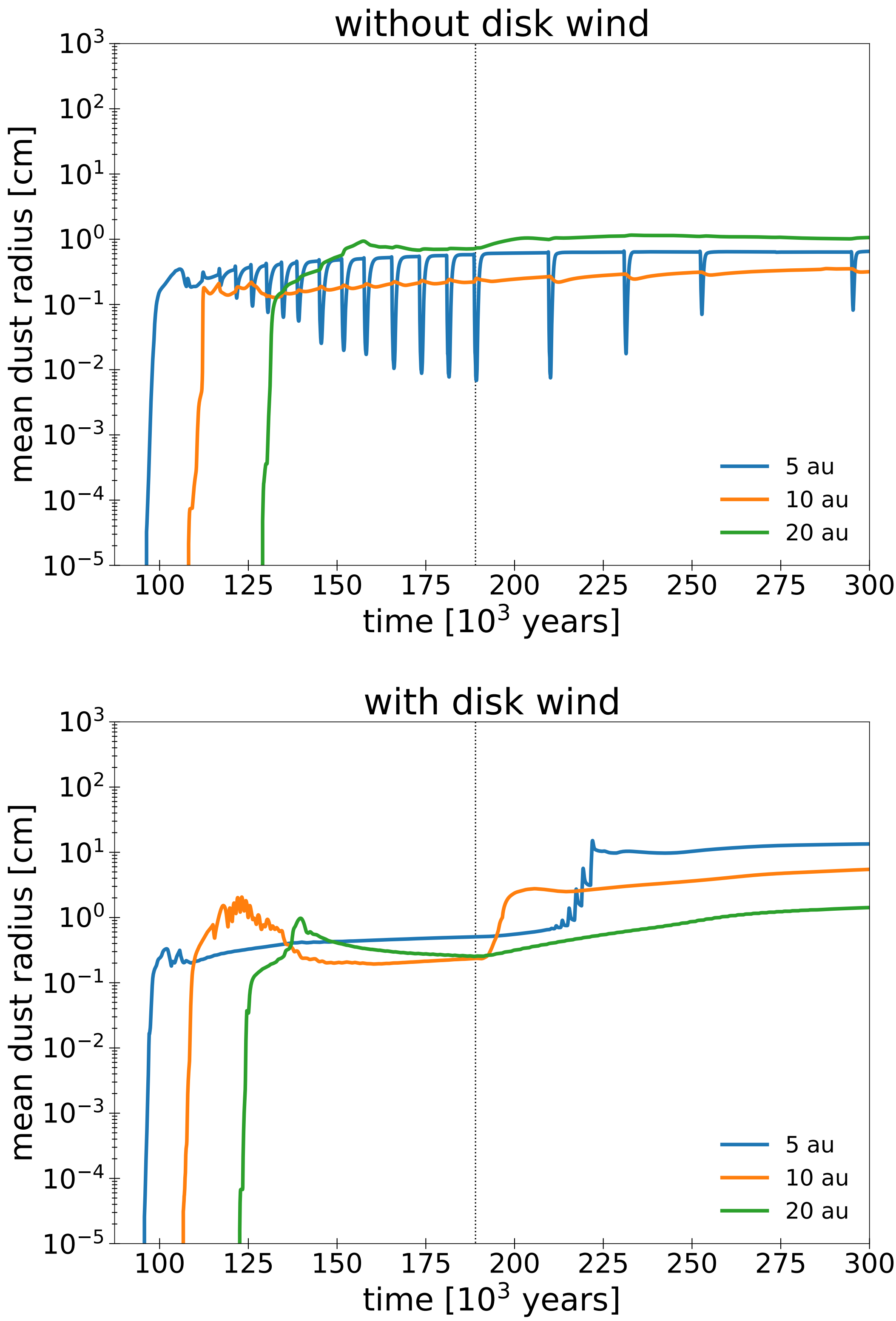

Figure 24. Time evolution of the mean dust size at 5 au, 10 au, and 20 au. The upper and lower panels show the case with and without disk wind, respectively.

4 Discussion

4.1 Possibility of streaming instability

In this section, I explore the application of the results obtained in this study to the process of planet formation. Streaming instability is considered the mechanism for the accumulation of dust in the disk (Youdin & Goodman 2005; Johansen & Youdin 2007; Carrera et al. 2015; Yang et al. 2017). This instability arises from the aerodynamic interaction between gas and dust and the effects of rotation (Lesur et al. 2023). The results of multidimensional numerical simulations confirm the local accumulation of dust due to this instability. From these simulations, the conditions for streaming instability are evaluated based on the mass ratio between dust and gas surface density, $Z = \Sigma_{\rm d}/\Sigma_{\rm g}$. Li & Youdin (2021) expresses the conditions under which streaming instability occurs based on the their results of numerical simulations with the following formula,

$$\log\left(\frac{Z_{\rm crit}}{\Pi}\right) = \begin{cases} 0.1\,(\log {\rm St})^2 + 0.32\log {\rm St} - 0.24 & ({\rm St} < 0.015) \\ 0.13\,(\log {\rm St})^2 + 0.1\log {\rm St} - 1.07 & ({\rm St} > 0.015) \end{cases} \tag{83}$$

where $Z_{\rm crit}$ is the critical mass ratio and Π represents the effect of the pressure gradient force and is described as

$$\Pi = \frac{\eta r \Omega}{c_s}. \tag{84}$$

If the condition $Z > Z_{\rm crit}$ is realized, the Streaming instability occurs. Applying these criteria to the results of this study, I evaluate whether streaming instability occurs in the disk. Using the results of the disk evolution from this study, I calculate the dust-to-gas mass ratio (Σ) and average Stokes number at each time for radii of 5 au, 10 au, and 20 au. The average Stokes number is determined based on the average dust particle mass (see Section 3.3.3). Then, I plot the evolution curves for each radius (5, 10, 20 au) on a plane with mass ratio and Stokes number as axes, evaluating the possibility of streaming instability.

Figure 25 plots the evolution curves at each time for radii of 5 au, 10 au, and 20 au in the case without disk wind. The horizontal axis of the figure represents the Stokes number, and the vertical axis represents the dust-to-gas mass ratio divided by Π. The dashed lines represent the critical condition of streaming instability (83). As a time reference, markers are plotted on the evolution curves at 1.5×10^5 years, 2.0×10^5 years, 2.5×10^5 years, and 3.0×10^5 years, respectively. If each evolution

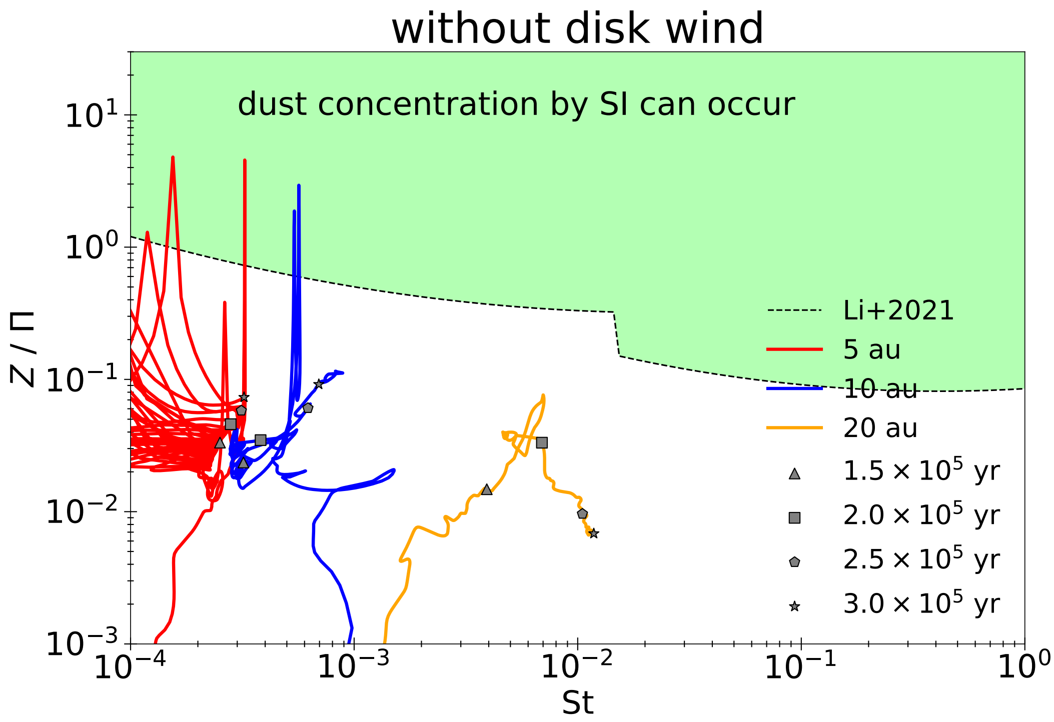

Figure 25. The evolution curves at each time for radii of 5 au, 10 au, and 20 au in the calculation without a disk wind. The horizontal and vertical axes represent the Stokes number and the gas-to-dust mass ratio divided by Π, respectively. The dashed lines represent the critical condition of streaming instability (83).

curve remains in the region above the dashed lines for a sufficient duration, it is considered that there is a possibility of the occurrence of streaming instability.

In the case without disk wind, the evolution curves for 5 au and 10 au exist in regions where streaming instability could occur. I confirm that the time that the curves spend in the region where streaming instability is likely to occur is about 50 years. On the other hand, the time for dust accumulation due to streaming instability is estimated to be $10^2 - 10^3\Omega^{-1} \sim 10^2 - 10^3$ years (Li & Youdin 2021; Tominaga & Tanaka 2023). In other words, the time during which the evolution curves exist in the region where streaming instability could occur is shorter than the time it takes for streaming instability to grow and dust accumulation to occur. Therefore, in the case without disk wind, it is considered that dust accumulation due to streaming instability does not occur within the calculation time of this study, and planet formation is not promoted.

Next, I examine the possibility of dust accumulation due to streaming instability in the case with disk wind. Figure 26 is the same as Figure 25 but for the case with disk wind. Each evolution curve at different radii exists within the region where streaming instability can occur. For the evolution curves of 10 au and 20 au, it is difficult for dust accumulation to occur due to streaming instability for the same

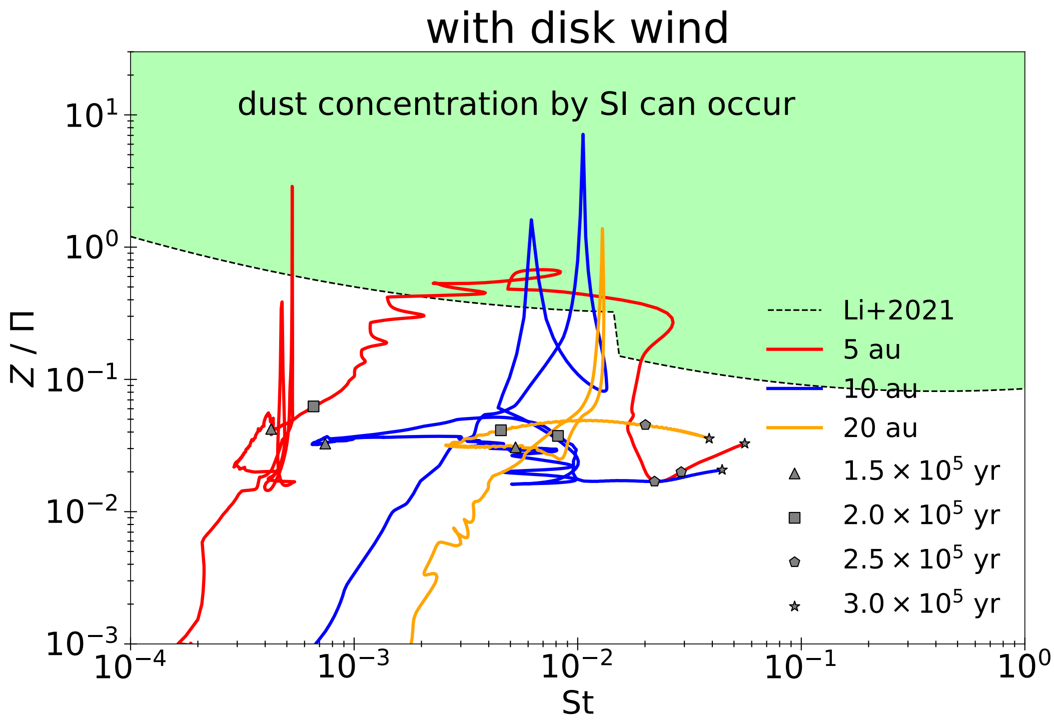

Figure 26. As Fig. 25 but for the case with a disk wind.

reasons as the case without disk wind. On the other hand, the evolution curve for 5 au spends $\sim 5 \times 10^3$ years in the region where streaming instability occurs. This duration is longer than that required for dust accumulation due to streaming instability. In other words, at 5 au, there is a high possibility of dust accumulation due to streaming instability. Therefore, it is considered that calculation with disk wind is more likely to lead to planet formation.

4.2 Effect of wind on the evolution of disk and star

In the star formation process, it is important to understand how much of the gas from the initial molecular cloud core becomes a star, which is closely related to the star formation efficiency. Observations of star-forming regions suggest that not all the mass of a prestellar cloud core is converted into a star (André et al. 2010; Könyves et al. 2015). To determine the star formation efficiency, it is necessary to consider the mass ejection rate from the molecular cloud core (Myers et al. 2023). The protostellar outflow or disk wind is thought to play an important role in determining the converted stellar mass fraction from the molecular cloud core (Machida & Matsumoto 2012).

In this study, the presence or absence of disk wind (outflow) caused differences in the star and disk mass. We initially set up a molecular cloud core of 1 $M_\odot$. In the case without the disk wind, the stellar mass at the end of the infall phase is 0.57 $M_\odot$. After the infall phase, the stellar mass continues to increase due to mass accretion from the disk. Since there is no mass ejection, all the remaining gas in the disk will eventually accrete to the star, meaning that the star formation efficiency is unity (100%). On the other hand, in the case with disk wind, the stellar mass at the end of the infall phase is 0.31 $M_\odot$ and 0.31 $M_\odot$ at the end of the calculation. As a result, in the case with disk wind, the star formation efficiency is expected to be $\sim$ 0.4–0.5 (40–50%) and is almost determined at the end of the infall phase.

The presence or absence of disk wind significantly affects the evolution of the stellar and disk masses. If the disk wind is not considered, the mass loss of the disk after the infall phase is slow and the disk mass is relatively large at the end of the calculation. On the other hand, when the disk wind is included, most of the disk mass is lost due to the disk wind. Since the star gains mass by accretion from the disk, the disk wind is essential in determining the final stellar mass. In this study, I have used only one set of parameters in our disk evolution calculation, including the disk wind. It is necessary to study the mass evolution of stars and disks with other parameters (Myers et al. 2023).

4.3 Comparison with other studies

This section compares the results of this study with previous studies on the evolution of the disk and the dust growth.

Takahashi & Muto (2018) calculated the evolution of a disk composed of gas and dust starting from the disk formation phase, including the disk wind. They assumed that the disk wind is driven only after the infall phase, the disk temperature is fixed, and the MRI viscosity is constant within the disk. Their calculations showed that during the infall phase, the surface density follows a constant power-law distribution, maintaining $Q \simeq 1$. In this study, since I solved the energy equation to obtain the disk temperature and treated the viscosity of MRI viscosity $\alpha_{\rm MRI}$ as a function of the temperature, I could reproduce the episodic accretions or outbursts. Furthermore, I considered that the disk wind is also driven during the infall phase and showed that the disk wind significantly influences the activity of the outbursts and the evolution of the disk.

Takahashi & Muto (2018) showed that the disk wind removes gas from the inner disk region and eventually forms a hole structure in a protoplanetary disk. The dust particles then accumulate around the pressure maxima, leading to the formation of dust rings. However, while the wind model adopted in Takahashi & Muto (2018) considered mass loss from the disk, removal of angular momentum from the disk by the wind torque was ignored (see also Suzuki et al. 2010; Pinilla et al. 2016).

In this study, I examined the disk evolution considering both mass loss due to the disk wind and angular momentum transport due to the wind torque. The surface density decreases due to the disk wind, while the mass accretion driven by the wind torque replenishes the surface density. Therefore, considering the angular momentum transport by the disk wind, the formation of pressure maxima is less likely. However, in this study, the strength of the disk wind was assumed to be constant, whereas in reality, the wind strength is determined by the strength and configuration of the magnetic field and the degree of coupling between the gas and the magnetic field at each radius, as described in Section 4.4. If the wind strength varies across the disk, it should be possible to form local pressure maxima.

Tsukamoto et al. (2017) calculated the dust growth in a steady gas disk using the single-size approximation (Sato et al. 2016; Okuzumi et al. 2016). Their gas disk model is assumed to be gravitationally unstable. They showed that icy dust particles can significantly grow in the inner disk regions and the surface density of dust decreases due to the radial drift. On the other hand, our results differ from theirs, although it is necessary to note that our calculations consider the gas evolution including the mass supply onto the disk from the infalling envelope. In our calculations, during the infall phase, icy dust particles outside the snowline have their size limited by radial drift before collisional growth. Inside the snowline, the growth of dust particles is prevented by collisional fragmentation. Furthermore, Homma & Nakamoto (2018) notes that the treatment of frictional laws of dust particles can alter the time-scale of radial drift, thereby affecting dust growth. Therefore, it is essential to pay attention to the models of disk and dust motion in the evolution of the disk.

Xu & Armitage (2023) calculated the dust growth in a steady disk assumed to be gravitationally unstable. Unlike Tsukamoto et al. (2017), they solved for the evolution of the dust size distribution, considering fragmentation. Their fragmentation model is constructed based on the model proposed by Windmark et al. (2012a), which is derived from lab experiments. They demonstrated that through the mass increase by collisions between larger and smaller dust particles at high velocities, dust particles can overcome the fragmentation barrier, and grow to cm-size. In contrast, in this study, we construct the fragmentation model based on collisional numerical calculations (Wada et al. 2013). Despite differences in the fragmentation model, there is agreement that dust particles grow within the disk during the infall phase (Class 0/I phase).

Homma & Nakamoto (2018) calculated the gas and dust evolution from the disk formation stage. They considered the dust growth including the porosity evolution of dust particles based on Okuzumi et al. (2012). They argued that in the building phase of the disk, since the growth of icy dust particles is prevented by radial drift, the planetesimal formation via direct collisional growth of dust particles is challenging. While the porosity evolution of dust particles is not considered in this study, in the region outside the snowline, the growth of icy dust particles is inhibited by radial drift. This result is consistent with Homma & Nakamoto (2018). In our calculations, during the infall phase, there is little impact of the disk wind on the dust growth. On the other hand, differences in dust growth between the case without and with a disk wind are seen after the infall phase. In the case with disk wind, the region where icy dust particles can exist expands with decreasing disk temperature. Therefore, the consideration of the porosity evolution of dust particles is expected to become more crucial for collisional coagulation after the infall phase. especially in the case with disk wind.

4.4 Uncertainties and caveats

In this study, I have fixed some physical quantities related to the initial molecular cloud core. If the properties of the molecular cloud core are changed, then the properties of the disks should also be changed. I plan to perform calculations with different molecular cloud core parameters to investigate the effect on disk evolution in future studies and we discuss possible changes in the disk properties in this subsection.

I have adopted the magnetically driven wind model used in Tabone et al. (2022). In the model, the disk wind is characterized by two parameters $\alpha_{\rm DW}$ and λ, which are set to be constant in time and space. The strength of the magnetically driven wind depends on the strength and configuration of the magnetic field (Blandford & Payne 1982; Machida & Hosokawa 2020). Assuming that the magnetic torque term is dominant in the wind parameter and $B_\phi = b_m B_z$, $\alpha_{\rm DW}$ is estimated as

$$\alpha_{\rm DW} \simeq 10^{-3} \left(\frac{b_m}{1}\right) \left(\frac{\epsilon}{10^{-1}}\right)^{-1} \left(\frac{\beta}{10^4}\right)^{-1}, \tag{85}$$

where $\epsilon = h_g/r$ is the disk aspect ratio and $\beta = 8\pi P/B^2$ is the plasma beta. Equation (85) implies that a highly inclined field and a relatively strong magnetic field are required for a larger value of $\alpha_{\rm DW}$, which was used in this study.

The magnetic lever arm parameter λ depends on the strength and configuration of the magnetic field. Theoretical and observational studies can determine the value of λ in the range $\lambda = 1.6$– 5 (Anderson et al. 2003; Pudritz & Ray 2019; Tabone et al. 2022). This study uses a constant value $\lambda = 2$, as described in Section 2.7. Recently, observations have found multiple nested outflow structures, implying that the value of λ varies spatially (Harada et al. 2023; Omura et al. 2024). When considering the more realistic disk evolution with the disk wind, it is crucial to understand the distribution and evolution of the parameters controlling the disk wind.

The efficiency of the angular momentum transport by MRI, especially in the dead zone, is set to be constant in time and space as $\alpha_{\rm MRI,dead} = 10^{-4}$. However, the parameter $\alpha_{\rm MRI,dead}$ could be affected by the magnetic field strength and non-ideal magnetohydrodynamic effects (Sano et al. 2000; Bai 2011; Lesur 2021). In the case with disk wind, the surface density of the disk becomes low in the later stage, allowing ionization sources such as cosmic rays to penetrate the interior of the disk. Thus, the ionization degree should increase in such a disk.

On the other hand, dust particles can adsorb charged particles in the gas phase on their surface, thereby reducing the abundance of charged particles (Umebayashi & Nakano 1990; Sano et al. 2000; Koga et al. 2019; Kawasaki et al. 2022; Kawasaki & Machida 2023). The coagulation growth of dust particles in the disk decreases the dust abundance, and the adsorption efficiency of charged particles also decreases (Delage et al. 2023). Thus, the dust growth increases the ionization degree, and MRI can become active. Thus, for a more realistic calculation, it is necessary to consider the coevolution of dust particles and the MRI turbulence strength.

As a mechanism of disk dissipation, photoevaporation by stellar irradiation has been extensively studied. The mass loss rate of the disk due to photoevaporation is estimated to be 10^{-10}–10^{-8} $\mathrm{M_\odot\ yr^{-1}}$ (Alexander et al. 2006; Owen et al. 2010; Tanaka et al. 2013), depending on the stellar mass and the flux at each wavelength. In our calculations, the disk dissipates with a mass loss rate of $\dot{M}_{\rm wind} \simeq 10^{-8}$–$10^{-7}$ $\mathrm{M_\odot\ yr^{-1}}$ by the disk wind after the infall phase. The mass loss rate due to disk wind decreases with time. Thus, the mass loss rate by photoevaporation should exceed that by the disk wind in the final stage of disk evolution. Therefore, we need to consider photoevaporation to thoroughly investigate the disk dissipation process.

5 Conclusions

In this study, I investigated the early evolutionary stage of protoplanetary disk and dust growth, considering a disk wind. I constructed a one-dimensional disk evolution model of gas and dust beginning from the disk formation stage, mainly based on Takahashi et al. (2013). In addition to the infall onto the disk from the core or the infalling envelope, I incorporated the magnetically driven disk wind model proposed by Tabone et al. (2022) into the disk evolution model. I calculated not only the spatial evolution of dust particles but also the evolution of dust size distribution. I calculated the cases with and without disk wind and compared the disk evolution and dust growth between these cases.

When the disk wind is not considered, the episodic accretions (or outbursts) occur, as seen in previous studies (e.g., Vorobyov & Basu 2006), and continue until the end of the calculation (3.0×10^5 years). The disk surface density and temperature profile vary significantly in the inner disk region due to the recurrent outbursts. For the outer disk region, the angular momentum is transported by gravitational torque and the disk expands, and the disk extends outward with time. The disk mass is relatively massive even at the end of the calculation in the case without disk wind.

In the calculation with the disk wind, the episodic accretions (or outbursts) also occur recurrently as in the case without disk wind. The interval between outbursts is shorter than in the case without disk wind. After the infall phase, the disk mass gradually decreases and the outbursts are quenched. The disk wind extracts mass from the disk and thus has a significant impact on the evolution of stellar mass. The star and disk mass are smaller than in the case without disk wind.

During the infall phase, the presence of a disk wind did not show a significant difference in dust size evolution compared to the case without disk wind. Dust particles grow to approximately 1-10 cm in the entire disk during the infall phase. The maximum size of dust particles was determined by different constraints inside and outside the H_2O snowline. Inside the H_2O snowline, the maximum size of dust particles is limited by the collisional fragmentation of dust particles. On the other hand, outside the snowline, the maximum dust size is constrained by the radial drift of dust particles.

After the infall phase, the presence or absence of a disk wind resulted in differences in dust particle size evolution. In the case without disk wind, the snowline remained outside of 10 au, and there was little change in the dust size during the infall phase. On the other hand, in the case with disk wind, the disk temperature decreases due to a disk wind, and the snowline migrates inward. As a result, the dust particles can grow larger than 10 cm. Therefore, it is found that a disk wind is important for dust growth or planet formation after the infall phase.

acknowledge

I would like to express my gratitude to Professor Masahiro Machida for his appropriate and thoughtful guidance during my research activities and paper writing. Additionally, I am thankful to everyone in the same laboratory for their support in various situations.

REFERENCES

Adachi I., Hayashi C., Nakazawa K., 1976, Progress of Theoretical Physics, 56, 1756

Alexander R. D., Clarke C. J., Pringle J. E., 2006, MNRAS, 369, 229

Anderson J. M., Li Z.-Y., Krasnopolsky R., Blandford R. D., 2003, ApJ, 590, L107

André P., et al., 2010, A&A, 518, L102

Andrews S. M., et al., 2018, ApJ, 869, L41

Arakawa S., Tanaka H., Kokubo E., Nishiura D., Furuichi M., 2023a, A&A, 670, L21

Arakawa S., Okuzumi S., Tatsuuma M., Tanaka H., Kokubo E., Nishiura D., Furuichi M., Nakamoto T., 2023b, ApJ, 951, L16

Bae J., Hartmann L., Zhu Z., Gammie C., 2013, ApJ, 764, 141

Bae J., Hartmann L., Zhu Z., Nelson R. P., 2014, ApJ, 795, 61

Bai X.-N., 2011, ApJ, 739, 50

Bai X.-N., 2016, ApJ, 821, 80

Balbus S. A., Hawley J. F., 1992, ApJ, 400, 610

Birnstiel T., Dullemond C. P., Brauer F., 2010, A&A, 513, A79

Birnstiel T., Klahr H., Ercolano B., 2012, A&A, 539, A148

Blandford R. D., Payne D. G., 1982, MNRAS, 199, 883

Blum J., Münch M., 1993, Icarus, 106, 151

Bonnor W. B., 1956, MNRAS, 116, 351

Booth R. A., Meru F., Lee M. H., Clarke C. J., 2018, MNRAS, 475, 167

Brauer F., Dullemond C. P., Henning T., 2008, A&A, 480, 859

Carrera D., Johansen A., Davies M. B., 2015, A&A, 579, A43

Cassen P., Moosman A., 1981, Icarus, 48, 353

Coradini A., Magni G., Federico C., 1981, A&A, 98, 173

Delage T. N., Gárate M., Okuzumi S., Yang C.-C., Pinilla P., Flock M., Stammler S. M., Birnstiel T., 2023, A&A, 674, A190

Desch S. J., Turner N. J., 2015, ApJ, 811, 156

Dominik C., Tielens A. G. G. M., 1997, ApJ, 480, 647

Ebert R., 1955, Z. Astrophys., 37, 217

Flock M., Fromang S., Turner N. J., Benisty M., 2016, ApJ, 827, 144

Gammie C. F., 1996, ApJ, 457, 355

Garaud P., Meru F., Galvagni M., Olczak C., 2013, ApJ, 764, 146

Glassgold A. E., Najita J., Igea J., 1997, ApJ, 480, 344

Harada N., et al., 2023, ApJ, 945, 63

Hasegawa Y., Suzuki T. K., Tanaka H., Kobayashi H., Wada K., 2021, ApJ, 915, 22

Hasegawa Y., Suzuki T. K., Tanaka H., Kobayashi H., Wada K., 2023, ApJ, 944, 38

Homma K., Nakamoto T., 2018, ApJ, 868, 118

Hueso R., Guillot T., 2005, A&A, 442, 703

Igea J., Glassgold A. E., 1999, ApJ, 518, 848

Inutsuka S.-i., 2012, Progress of Theoretical and Experimental Physics, 2012, 01A307

Johansen A., Youdin A., 2007, ApJ, 662, 627

Johansen A., Oishi J. S., Mac Low M.-M., Klahr H., Henning T., Youdin A., 2007, Nature, 448, 1022

Kataoka A., Tanaka H., Okuzumi S., Wada K., 2013, A&A, 557, L4

Kawasaki Y., Machida M. N., 2023, MNRAS, 522, 3679

Kawasaki Y., Koga S., Machida M. N., 2021, MNRAS, 504, 5588

Kawasaki Y., Koga S., Machida M. N., 2022, MNRAS, 515, 2072

Kobayashi H., Tanaka H., 2010, Icarus, 206, 735

Kobayashi H., Tanaka H., 2021, ApJ, 922, 16

Koga S., Machida M. N., 2023, MNRAS, 519, 3595

Koga S., Tsukamoto Y., Okuzumi S., Machida M. N., 2019, MNRAS, 484, 2119

Koga S., Kawasaki Y., Machida M. N., 2022, MNRAS, 515, 6073

Könyves V., et al., 2015, A&A, 584, A91

Kudoh T., Shibata K., 1997, ApJ, 474, 362

Langkowski D., Teiser J., Blum J., 2008, ApJ, 675, 764

Lebreuilly U., Commerçon B., Laibe G., 2019, A&A, 626, A96

Lebreuilly U., Commerçon B., Laibe G., 2020, A&A, 641, A112

Lesur G., 2021, Journal of Plasma Physics, 87, 205870101

Lesur G., et al., 2023, in Inutsuka S., Aikawa Y., Muto T., Tomida K., Tamura M., eds, Astronomical Society of the Pacific Conference Series Vol. 534, Astronomical Society of the Pacific Conference Series. p. 465

Li R., Youdin A. N., 2021, ApJ, 919, 107

Liu Y., Takahashi S., Machida M., Tomisaka K., Girart J. M., Ho P. T. P., Nakanishi K., Sato A., 2023, arXiv e-prints, p. arXiv:2312.13573

Machida M. N., Basu S., 2019, ApJ, 876, 149

Machida M. N., Hosokawa T., 2020, MNRAS, 499, 4490

Machida M. N., Matsumoto T., 2011, MNRAS, 413, 2767

Machida M. N., Matsumoto T., 2012, MNRAS, 421, 588

Machida M. N., Matsumoto T., Hanawa T., Tomisaka K., 2006, ApJ, 645, 1227

Machida M. N., Inutsuka S.-i., Matsumoto T., 2010, ApJ, 724, 1006

Marchand P., Lebreuilly U., Mac Low M. M., Guillet V., 2023, A&A, 670, A61

Myers P. C., Dunham M. M., Stephens I. W., 2023, ApJ, 949, 19

Nakamoto T., Nakagawa Y., 1994, ApJ, 421, 640

Ohashi S., et al., 2021, ApJ, 907, 80

Ohashi N., et al., 2023a, ApJ, 951, 8

Ohashi S., et al., 2023b, ApJ, 954, 110

Okuzumi S., Tanaka H., Sakagami M.-a., 2009, ApJ, 707, 1247

Okuzumi S., Tanaka H., Kobayashi H., Wada K., 2012, ApJ, 752, 106

Okuzumi S., Momose M., Sirono S.-i., Kobayashi H., Tanaka H., 2016, ApJ, 821, 82

Omura M., Tokuda K., Machida M. N., 2024, arXiv e-prints, p. arXiv:2401.03086

Ormel C. W., Cuzzi J. N., 2007, A&A, 466, 413

Ormel C. W., Spaans M., Tielens A. G. G. M., 2007, A&A, 461, 215

Owen J. E., Ercolano B., Clarke C. J., Alexander R. D., 2010, MNRAS, 401, 1415

Pinilla P., Flock M., Ovelar M. d. J., Birnstiel T., 2016, A&A, 596, A81

Pudritz R. E., Ray T. P., 2019, Frontiers in Astronomy and Space Sciences, 6, 54

Ruden S. P., Pollack J. B., 1991, ApJ, 375, 740

Sano T., Miyama S. M., Umebayashi T., Nakano T., 2000, ApJ, 543, 486

Sato T., Okuzumi S., Ida S., 2016, A&A, 589, A15

Shakura N. I., Sunyaev R. A., 1973, A&A, 24, 337

Sheehan P. D., Tobin J. J., Federman S., Megeath S. T., Looney L. W., 2020, ApJ, 902, 141

Shoshi A., et al., 2023, arXiv e-prints, p. arXiv:2312.02504

Smoluchowski M. V., 1916, Zeitschrift fur Physik, 17, 557

Stammler S. M., Birnstiel T., 2022, ApJ, 935, 35

Suzuki T. K., Muto T., Inutsuka S.-i., 2010, ApJ, 718, 1289

Suzuki T. K., Ogihara M., Morbidelli A., Crida A., Guillot T., 2016, A&A, 596, A74

Tabone B., Rosotti G. P., Cridland A. J., Armitage P. J., Lodato G., 2022, MNRAS, 512, 2290

Takahashi S. Z., Muto T., 2018, ApJ, 865, 102

Takahashi S. Z., Inutsuka S.-i., Machida M. N., 2013, ApJ, 770, 71

Tanaka K. E. I., Nakamoto T., Omukai K., 2013, ApJ, 773, 155

Testi L., et al., 2014, in Beuther H., Klessen R. S., Dullemond C. P., Henning T., eds, Protostars and Planets VI. pp 339–361 (arXiv:1402.1354), doi:10.2458/azu_uapress_9780816531240-ch015

Tokuda K., et al., 2020, ApJ, 899, 10

Tomida K., Tomisaka K., Matsumoto T., Hori Y., Okuzumi S., Machida M. N., Saigo K., 2013, ApJ, 763, 6

Tomida K., Machida M. N., Hosokawa T., Sakurai Y., Lin C. H., 2017, ApJ, 835, L11

Tominaga R. T., Tanaka H., 2023, ApJ, 958, 168

Tsukamoto Y., Okuzumi S., Kataoka A., 2017, ApJ, 838, 151

Tsukamoto Y., Machida M. N., Susa H., Nomura H., Inutsuka S., 2020, ApJ, 896, 158

Tsukamoto Y., Machida M. N., Inutsuka S., 2021a, ApJ, 913, 148

Tsukamoto Y., Machida M. N., Inutsuka S.-i., 2021b, ApJ, 920, L35

Tsukamoto Y., Machida M. N., Inutsuka S.-i., 2023, PASJ, 75, 835

Ueda T., Flock M., Okuzumi S., 2019, ApJ, 871, 10

Umebayashi T., Nakano T., 1990, MNRAS, 243, 103

Vorobyov E. I., Basu S., 2006, ApJ, 650, 956

Wada K., Tanaka H., Suyama T., Kimura H., Yamamoto T., 2009, ApJ, 702, 1490

Wada K., Tanaka H., Okuzumi S., Kobayashi H., Suyama T., Kimura H., Yamamoto T., 2013, A&A, 559, A62

Wardle M., Salmeron R., 2012, MNRAS, 422, 2737

Weidenschilling S. J., 1977, MNRAS, 180, 57

Whipple F. L., 1972, in Elvius A., ed., From Plasma to Planet. p. 211

Windmark F., Birnstiel T., Güttler C., Blum J., Dullemond C. P., Henning T., 2012a, A&A, 540, A73

Windmark F., Birnstiel T., Ormel C. W., Dullemond C. P., 2012b, A&A, 544, L16

Wurm G., Paraskov G., Krauss O., 2005, Icarus, 178, 253

Xu W., Armitage P. J., 2023, ApJ, 946, 94

Xu W., Kunz M. W., 2021a, MNRAS, 502, 4911

Xu W., Kunz M. W., 2021b, MNRAS, 508, 2142

Yang C.-C., Johansen A., Carrera D., 2017, A&A, 606, A80

Youdin A. N., Goodman J., 2005, ApJ, 620, 459

Youdin A. N., Lithwick Y., 2007, Icarus, 192, 588

Zhu Z., Hartmann L., Gammie C., 2010, ApJ, 713, 1143

Zhu Z., Hartmann L., Nelson R. P., Gammie C. F., 2012, ApJ, 746, 110